North American Climate in CMIP5 Experiments:

Part III: Assessment of 21st Century Projections

Eric D. Maloney[1]*, Suzana J. Camargo[2], Edmund Chang[3], Brian Colle[3], Rong Fu[4], Kerrie L. Geil[5], Qi Hu[6], Xianan Jiang[7], Nathaniel Johnson[8], Kristopher B. Karnauskas[9], James Kinter[10,12], Benjamin Kirtman[11], Sanjiv Kumar[12], Baird Langenbrunner[13], Kelly Lombardo[3], Lindsey N. Long[13,14], Annarita Mariotti[15], Joyce E. Meyerson[13], Kingtse C. Mo[13], J. David Neelin[13], Zaitao Pan[16], Richard Seager[17], Yolande Serra[5], Anji Seth[18], Justin Sheffield[19], Julienne Stroeve[20], Jeanne Thibeault[18], Shang-Ping Xie[8], Chunzai Wang[21], Bruce Wyman[22], and Ming Zhao[22]

[1.] *Department of Atmospheric Science, Colorado State University, Fort Collins, CO*

[2.] *Lamont-Doherty Earth Observatory, Columbia University, Palisades, NY*

[3.] *School of Marine and Atmospheric Sciences, Stony Brook University - SUNY*

[4.] *Department of Geological Sciences, University of Texas, Austin, TX*

[5.] *Department of Atmospheric Sciences, University of Arizona, Tucson, AZ*

[6.] *Department of Earth and Atmospheric Sciences, University of Nebraska, Lincoln, Lincoln, NE*

[7.] *Joint Institute for Regional Earth System Science & Engineering, Univ. of California, Los Angeles, CA*

[8.] *International Pacific Research Center, University of Hawaii, Honolulu, Hawaii*

[9.] *Woods Hole Oceanographic Institution, Woods Hole, MA*

[10.] *Atmospheric, Oceanic & Earth Sciences Dept., George Mason University, Fairfax, VA*

[11.] *Division of Meteorology and Physical Oceanography, University of Miami, Miami, FL*

[12.] *Center for Ocean-Land-Atmosphere Studies, Calverton, MD*

[13.] *Department of Atmospheric and Oceanic Sciences, University of California, Los Angeles*

[13.] *Climate Prediction Center/NCEP/NWS/NOAA, Camp Springs, MD*

[14.] *Wyle Laboratories, McLean, VA*

[15.] *NOAA Climate Program Office, Silver Spring, MD*

[16.] *Department of Earth and Atmospheric Sciences, St. Louis University, St. Louis, MO*

[17.] *Lamont-Doherty Earth Observatory, Palisades, NY*

[18.] *Department of Geography, University of Connecticut, Storrs, CT*

[19.] *Department of Civil & Environmental Engineering, Princeton University, Princeton, NJ*

[20.] *National Snow and Ice Data Center, University of Colorado, Boulder, CO*

[21.] *Atlantic Oceanographic and Meteorological Laboratory, Miami, FL*

[22.] *Geophysical Fluid Dynamics Laboratory, Princeton, NJ*

Journal of Climate

Submitted July 30, 2012

*Corresponding author address: Eric D. Maloney, Department of Atmospheric Science, Colorado State University, 1371 Campus Delivery, Fort Collins, CO 80523-1371. Email: emaloney@atmos.colostate.edu

Abstract

In Part 3 of a three-part study on North American climate in Coupled Model Intercomparison project (CMIP5) models, we examine projections of 21st Century climate in the RCP4.5 and RCP8.5 emission experiments. Aspects of North American climate change that are examined include changes in continental-scale temperature and the hydrologic cycle, extremes events, and storm tracks, as well as regional manifestations of these climate variables. We also examine changes in east Pacific and Atlantic tropical cyclone activity and North American intraseasonal to decadal variability, including changes in teleconnections to other regions of the globe.

Projected changes are generally consistent with those in CMIP3, although with better model agreement in some areas (e.g. projections of summer time precipitation decreases in the Caribbean and Southern Mexico). Although many projected changes in North American climate are robust across CMIP5 models, substantial disagreement in some areas helps to define priorities for future research. Areas of disagreement include projections of changes in snow water equivalent and diurnal temperature range on a regional basis, precipitation in the Southern U.S., Atlantic and east Pacific tropical cyclone activity, intraseasonal variability, and El Niño teleconnections. Model success in simulating historical climate as shown in Parts 1 and 2 of this study lend confidence to many of the projected results. However, model biases in other areas decrease confidence in projections, including changes in the timing of North American monsoon precipitation, growing season length along the West Coast, and the distribution of persistent drought and wet spells.

65 **1. Introduction**

66 The 21st century projections generated by the Coupled Model Intercomparison Project
67 (CMIP5, Taylor et al. 2012) are analyzed here to assess climate change in North America (NA).
68 This study accompanies two companion papers (Sheffield et al. 2012a,b) that assess CMIP5
69 models' potential to accurately simulate regional climate in the 20th century. This study will
70 begin with an examination of the changes in the continent-wide distribution of seasonal
71 precipitation and temperature in two emissions pathways. It will then focus on a select set of
72 regional climate features and their variability. These changes are considered in the context of the
73 ability of models to accurately simulate current climate. As noted by Sheffield et al. (2012a), the
74 ability of CMIP5 models to simulate current climate is generally comparable to that of CMIP3
75 models, with some improvement noted for individual models.

76 Projections of NA climate change have been conducted as part of previous climate
77 assessments (e.g. CMIP3). Some salient points will be briefly summarized here. By 2080-2099,
78 robust annual mean temperature increases are projected across NA with the greatest changes in
79 Northern Canada and Alaska where 10°C mean wintertime temperature increases are projected in
80 some scenarios (IPCC 2007). Robust increases in annual mean precipitation are projected for the
81 Northern tier of the U.S., northward into Canada, and with robust decreases for the Southwest
82 U.S., east Pacific warm pool, Caribbean, and adjacent land areas (e.g. Neelin et al. 2006; Seager
83 et al. 2007; Seager and Vecchi 2010).

84 Beyond mean state changes, CMIP3 models predict a general increase in precipitation
85 intensity (e.g. Diffenbaugh et al. 2005; Mahajan et al. 2012), particularly notable in the Northern
86 Tier of the U.S. and Canada (Tebaldi et al. 2006). Increases in the duration and severity of

drought have been projected to occur in regions such as Central America and midlatitude NA (e.g. Sheffield and Wood 2008), of which increased temperatures and evapotranspiration are major components (Francina et al. 2010; Gutzler and Robbins 2011; Wehner et al. 2011). A general increase in heat waves, decrease in cold extremes, decrease in frost days, and increase in length of the growing season have been projected across large portions of NA (Meehl and Tebaldi 2004; Diffenbaugh et al. 2005; Biasutti et al. 2012; Christiansen et al. 2011; Diffenbaugh and Scherer 2011; Duffy and Tebaldi 2012). Decreases in the duration of the snowpack have been projected for many regions, in particular low altitude areas of the Pacific Northwest and Rockies (e.g. Brown and Mote 2009; Elsner et al. 2010). Such changes are projected to lead to earlier Spring snowmelt in many areas of the West (e.g. Hay et al. 2011). While model agreement is good on projected overall snow water equivalent declines in many areas by the end of the 21st century, some models show increases in snowpack along the Arctic Rim by 2100 (e.g. Hayhoe et al. 2004; Brown and Mote 2009), particularly at the height of the winter season even though the length of the snow season shortens (e.g. Raisanen 2008).

The projected response of NA climate in future emission scenarios is often more nuanced on the regional and local scales than for the continental scale features, especially when considering the evolution during the seasonal cycle. For example, Rauscher et al. (2008) noted an earlier onset of the midsummer drought in Mexico and Central America in model projections for the end of the 21st century. Previous studies project a redistribution of precipitation in monsoon regimes such as the SW U.S. with reduced Spring rainfall, and increased late rainy season rainfall (Seth et al. 2010, 2011; Biasutti and Sobel 2009). Ruiz-Barradas and Nigam (2010) showed that projections for the 21st century indicate a wetter north central U.S. during

Spring (increase in number of extreme Springs) and a drier SW U.S., but little consistency in summer rainfall tendencies among models in these same regions. The uncertainty in projected summer precipitation extends to adjacent land areas of the Gulf of Mexico (Biasutti et al. 2011). Changes in North Atlantic tropical cyclone activity are uncertain, as climate models produce differing patterns of tropical SST change, and different representations of tropical Atlantic SST relative to the tropical mean, which is a strong regulator of Atlantic hurricane activity (e.g. Knutson et al. 2010; Zhao and Held 2012). Past studies using CMIP3-class models have generally indicated that climate projections for the 21st Century at the local and regional levels remain a substantial challenge.

The present study provides a summary of projected 21st Century NA climate change in the updated state-of-the-art climate and Earth system models of CMIP5. The results contained herein are contributed by individual members of the CMIP5 Task Force of the National Oceanographic and Atmospheric Administration (NOAA) Modeling Analysis and Prediction Program (MAPP), and reflect each researcher's individual expertise. Where appropriate, we make reference to individual papers submitted to this *Journal of Climate* special collection in parallel with this comprehensive study, and these individual contributions provide further depth to the findings that are summarized here.

Section 2 provides a brief introduction to the CMIP5 modeling project a well as the climate change experiments assessed. Section 3 presents an assessment of continental climate changes over the 21st Century. Section 4 assesses regional climate changes. How intraseasonal variability changes in the 21st Century is assessed in Section 5. Changes in Atlantic and east Pacific tropical cyclone activity are examined in Section 6. Multidecadal trends in interannual to decadal

131 hydroclimate variability are analyzed in Section 7. Conclusions are presented in Section 8.

132 **2. CMIP5 Models and Experiments**

133 We use projections from the CMIP5 multimodel dataset of historical climate and climate
134 change experiments (Taylor et al. 2012). The experiments include both decadal predictions and
135 long-term century-scale projections of climate. Table 1 summarizes information on the models
136 used in this study. As noted in Taylor et al. (2012), one advantage provided by the CMIP5
137 experiments versus the CMIP3 effort is that the horizontal resolution of the atmospheric
138 components of the coupled models has significantly improved. About one third of the models
139 have atmospheric resolution of approximately 1.5^{o} latitude or less, an improvement over CMIP3,
140 as no model has resolution coarser than 3° latitude. This higher resolution is of some help in
141 examining regional hydroclimate variables over NA, although still coarser than would be
142 desirable in regions of complex topography and coastlines.

143 RCP8.5 and RCP4.5 will be highlighted, as they represent the core concentration
144 pathways used for the CMIP5 project (Taylor et al. 2012). These experiments represent high
145 concentration and moderate mitigation pathways in which radiative forcing due to anthropogenic
146 factors reaches 8.5 W m^{-2} and 4.5 W m^{-2} by 2100, respectively (e.g. Meinshausen et al. 2011,
147 Figure 4). Radiative forcing continues to grow beyond 2100 in RCP8.5, whereas in RCP4.5
148 stabilization at 4.5 W m^{-2} occurs around 2050 and remains fixed. In terms of the time evolution
149 and value of globally-averaged radiative forcing at 2100, these pathways most closely resemble
150 the A2 and B1 scenarios for CMIP3 used in the IPCC Assessment Report 4 (IPCC 2007, Figure
151 10.26). These climate change experiments will be compared to historical runs of the same

152 models in which they attempt to reproduce past climate from the mid 19th Century onward when
153 being forced by observed trace gases, natural and anthropogenic aerosols, solar forcing, and
154 other agents (Taylor et al. 2012). The number of models used in a particular analysis shown
155 below is often limited by availability of data at the time of this study or local storage space,
156 although we try to be as comprehensive as possible.
157
158 **3. Continental Climate**

159 *a. Temperature and precipitation*

160 We first examine projected changes on the continental scale at the end of the 21st Century
161 relative to the 20th Century climate. Sheffield et al. (2012a) noted that CMIP5 models have
162 success at the capturing the broad-scale features of NA surface temperature and precipitation in
163 current climate, although with some regional-scale biases. Figure 1 shows the 15-member
164 multimodel mean December-February (DJF) and July-August (JJA) precipitation changes during
165 2070-2099 for RCP8.5 relative to a 1961-1990 base period. Figure 2 shows the model agreement
166 on the precipitation changes.

167 Figures 1 and 2 indicate increases in ensemble mean wintertime precipitation along the
168 west coast of NA from California to Alaska, as well as along the NA East Coast from the mid
169 Atlantic states northward. Model agreement for these changes is high north of 40°N, where all
170 but one or two models agree on these changes for all locations. Comparison to a similar
171 ensemble of 15 CMIP3 models indicates that while the large-scale pattern of precipitation
172 increases at mid- to high- latitudes and precipitation decreases in the subtropics is similar
173 between the two intercomparisons, one notable difference is that the boundary between these

changes has shifted slightly south, yielding projected precipitation increases over parts of California in CMIP5 (Neelin et al., 2012). Summertime ensemble mean precipitation changes are characterized by higher precipitation amounts in Alaska and the Yukon, where the models all agree on the sign of the changes. All models also suggest precipitation increases along the Arctic coast across the entire length of NA. The multimodel mean indicates reduced summertime precipitation in the east Pacific warm pool and the Caribbean, with agreement of all models in the vicinity of major Caribbean islands, the Yucatan, and in Southwestern Mexico adjacent to the east Pacific warm pool. The agreement on these changes for the Caribbean and Mexico was high for CMIP3 models (e.g. Neelin et al. 2006) and is reinforced as a region of even higher intermodel agreement in CMIP5.

Figure 3 shows the comparable multimodel mean changes for surface temperature for RCP8.5 during JJA and DJF. As expected, warming is projected across all regions of NA, with the greatest warming concentrated during wintertime at high latitude regions, where multimodel mean temperature increases peak near 15^{o}C in the vicinity of Hudson Bay.

b. Moisture fluxes

CMIP5 model projected differences in vertically integrated moisture transport (MT) to 500 hPa (vectors) and its divergence (contours) are shown in Figure 4 for four coupled models, for RCP8.5 (2081-2100) minus historical (1981-2000) experiments. The MT is well simulated in these models in historical simulations (Sheffield et al. 2012a). While the number of models is too few to provide robust conclusions regarding changes in MT, this analysis provides process level support for model agreement/disagreement in precipitation projections . In summer, the models

196 suggest an increased transport in both (East coast and Great Plains) branches of moisture flow,
197 with a poleward intensification in the coastal branch associated with a poleward shift in moisture
198 convergence on the northwest flank of the Atlantic subtropical anticyclone and increased
199 moisture divergence to the south. The increased Great Plains flux is consistent with projected
200 strengthening of the Great Plains low-level jet, as described in more detail below. Three of the
201 four models show increased divergence in the northern plains during summer, and all show
202 increased divergence in the Pacific Northwest, where model agreement exists on precipitation
203 decrease exists (Figure 2).

204 In winter, the models indicate stronger MT from the Pacific into the Northwest, but the
205 latitude of the increased westerly transport is critical in determining whether much of California
206 is in a region of increased or decreased divergence. Agreement also exists that increased MT
207 would result in more convergence from the mid-Atlantic through eastern Canada, while the Gulf
208 coast and Florida would see increased divergence of moisture.

209

210 *c. Evapotranspiration and Runoff*

211 Future changes in precipitation and how it is partitioned into evaporation and runoff have
212 implications for water availability and the occurrence of extreme hydrological events such as
213 floods and droughts. Evaluations of CMIP3 projections showed that changes in precipitation
214 coupled with increasing atmospheric demand leads to drying of sub-tropical regions including
215 Central America and the southwestern US (Wang, 2005; Seager et al. 2007; Sheffield et al.,
216 2008), and increased potential for flooding because of more frequent and intense precipitation
217 events, changes in snow accumulation and melt timing, and changes in antecedent soil moisture

conditions (e.g. Hamlet and Lettenmaier, 2007; Das et al., 2011). Here we analyze changes in the terrestrial water budget on a regional basis by calculating 30-year averages in annual mean precipitation, evapotranspiration and runoff between 1971-2000 and 2071-2100 for 13 climate models for six regions of NA (Figure 5). Changes in water storage (i.e. surface water, soil moisture, groundwater, etc.) over the 30-year periods are assumed to be small compared to the other terms and so precipitation should balance the sum of evapotranspiration and runoff.

For western and eastern NA regions an increase is projected in the multi-model mean annual precipitation under RCP8.5, consistent with Figure 1. The precipitation increases in these regions are apportioned more to evapotranspiration than to runoff, although models tend to overestimate evapotranspiration in historical simulations (Sheffield et al. 2012a). In the central region, annual mean precipitation increases are more modest. In high latitudes (Alaska/Northwest Canada and Northeast Canada) the multi-model mean precipitation is projected to increase, consistent with Figure 1, and is mostly partitioned into increases in runoff, rather than evapotranspiration. In Central America, precipitation is projected to decrease with most of the decrease manifesting in decreasing runoff.

d. Snow

Reductions in snow cover extent and amount are expected in the future as a result of increasing temperatures modified by changes in precipitation and their seasonal interactions. This has important implications for water supply, hydropower generation, and ecosystems, and feedbacks with the underlying soil and permafrost (Lawrence and Slater, 2010) and to the atmosphere through changes in albedo (Qu and Hall, 2007). CMIP3 projections (Räisänen, 2008)

240 indicated that warming reduces the snow season length from both ends across NA, but mid-
241 winter snow water equivalent (SWE) is expected to increase in more northerly colder regions
242 because of increased winter snowfall, but decrease in more southerly regions where temperature
243 effects on precipitation phase and melting dominate over any changes in precipitation amount.
244 Changes in snow are calculated using the CMIP5 model SWE values. Figure 6 (top)
245 shows the seasonal cycle of changes between 2099-2070 and 1971-2000 in monthly mean SWE
246 averaged over NA for a set of nine models. All models project a decrease in SWE throughout the
247 year with maximum changes during the peak of the snow season in Jan-Apr. The MME mean
248 decrease in SWE averaged over NA is about -30mm (with an inter-model range of about 25mm)
249 in the spring and about -5mm in the summer time (range is about 10mm). Spatially, the majority
250 of NA (south of 70^{o}N) is projected to experience a decline in SWE where increasing
251 temperatures have a dominant effect by reducing the ratio of snowfall to rainfall and accelerating
252 melting (Figure 6, bottom). These reductions are concentrated in the Rocky Mountains to
253 southern Alaska, on the eastern provinces of Canada, and with a lower magnitude on the
254 Canadian Prairies. North of 70^{o}N, SWE is projected to increase due to increasing precipitation,
255 which outweighs the effects of increasing temperature. Uncertainties across models are likely
256 associated with differences in the temperature projections, to which modeled snow is highly
257 sensitive (Räisänen, 2008). At higher latitudes, the sign of the change is uncertain in transitional
258 regions because of the competing effects of increasing snowfall and warming temperatures, and
259 in regions of increasing SWE where the magnitude of the precipitation increase is also quite
260 uncertain.
261

262 *e. Growing season length*

263 Projected warming is likely to be associated with impacts on temperature sensitive flora
264 and fauna, as well as agriculture. We calculate changes in biophysical-relevant temperature
265 thresholds including the last spring freeze, first autumn freeze and the growing season length in
266 RCP8.5 at 2071-2100. By end of century the analysis of the 6 models (Figure 7) indicates that
267 the growing season will increase across the NA continent, although substantial variability in the
268 magnitude of these changes exists on a regional basis. The largest changes occur over the
269 western US and northern Mexico, where increases of 2 months or more are projected. It should
270 be noted that these same regions are characterized by some of the largest negative biases in
271 historical simulations (Sheffield et al. 2012a). In the central US and Canada, increases of about
272 3-6 weeks are projected. The lengthening of the growing season is caused by earlier last spring
273 freezes and later first autumn freezes (not shown), but the change in the former is generally
274 larger.

275

276 *f. Frost days*

277 Figure 8 shows the change in the number of frost days (FDs) simulated by six models at
278 2071-2100. Maximum changes of over 80 days are limited to coastal regions of southern Alaska
279 and western Canada. The rest of the continent shows changes of between 50 and 80 days in the
280 western third from the US western mountains up through the Canadian Rockies to Alaska, and
281 between 20 to 50 days over the eastern two thirds, with less change in the southern U.S.. Most
282 uncertainty exists across the model projections in the West with decreases that range from about
283 50-60 days for CCSM4 to more than 100 days for IPSL-CM5A-LR. The highest agreement is in

284 the Canadian Northern Territories and for central America. Some of the differences can be
285 explained by the historical biases in the models (Sheffield et al., 2012a), which may limit or
286 enhance future changes even if the projected shift in temperature is the same across models. For
287 example, CCSM4 has historically too few FDs in the central US, and projects less of a decrease
288 in this region in the future. The IPSL-CM5A-LR and CSIRO-MK3-6-0 models project the
289 largest decreases in FDs over the western U.S., but these two models also have the largest over-
290 estimation of historic FDs in this region. These results indicate that bias correction of the
291 modeled extreme values of these type can help reduce the uncertainty in future projections.
292
293 *g. Daily temperature range*
294 One robust global climate change signal over the 20th Century was the widespread
295 decline of daily temperature range (DTR), especially in winter, resulting from nighttime
296 temperatures warming faster than daytime (Karl et al. 1993, Dai et al 1999, Easterling et al 1997,
297 and Vose et al 2005). In RCP4.5, the CMIP5 models project sharp decreases in wintertime DTR
298 in the mid 21st Century, most prominent in an east-west oriented band at northern latitudes
299 where DTR decreases by more than 0.2 ^{o}C/decade (Figure 9). This decrease in DTR is largely
300 due to preferential increases in nighttime temperature. In the southern U.S. and Mexico, DTR is
301 projected to increase, although with larger uncertainty as indicated by the larger inter-model
302 variance. During summer, DTR is projected to slightly increase (<0.1 C/decade) in the north
303 central section of the U.S. In the southeastern U.S., the multimodel mean DTR signal is rather
304 weak, which is also accompanied by larger variance among the models. The uncertainty in
305 projected DTR trend is generally higher in the lower latitudes. If we view the signal (DTR trend)

306 to noise (inter-model variance) ratio as a simple measure of the confidence in the model
307 projections, the northern Rocky Mountain region has smallest uncertainty in future projections.
308
309 *h. Extreme events*

310 CMIP5 historical and RCP 4.5 projection experiments are examined to assess projected
311 changes in drought and persistent wet spells over the U.S.. The methodology used is the same as
312 in part 1 of this study (Sheffield et al. 2012a), and repeated in the Figure 10 caption. Five
313 models that contained three or more members for both the historical and projection experiments
314 were chosen to analyze the response of extreme events to an increase in CO_2. We first calculated
315 the difference in extreme precipitation event frequency of occurrence (FOC) when each
316 experiment's own climatology is used as a baseline. Each model shows little difference in the
317 FOCs for both positive and negative events (not shown). Based on the new projected
318 climatology, there is little change in the FOC pattern for both precipitation and soil moisture.
319 The results become more interesting when the historical climatology is used as to assess
320 future changes in dry and wet spells (Figure 10). Models tend to show a decrease in positive
321 (wet) events in Mexico and the southwest and an increase in positive (wet) events in the eastern
322 United States. The opposite is true for negative (dry) events. The CAN and IPSL, and MPI and
323 CCSM4 to a lesser extent, also show increases in positive events in the northwest and northern
324 Great Plains. These patterns of extreme event changes are consistent with differences in annual
325 mean precipitation for each model (not shown). It should be noted that model ability to simulate
326 the correct distribution of extreme precipitation event occurence in the current climate is limited
327 (Sheffield et al. 2012a).

328 Our analysis of extremes now extends to high temperatures using one ensemble member
329 for nine models for RCP4.5 and RCP8.5 at 2071-2100. Daily maximum surface temperatures
330 (T_{max}) are used to compute the number of days per year that exceed 90 F and 100 F, referred to
331 ND>90F and ND>100F, respectively.
332 For RCP4.5, all selected models project an increase of ND>90F across much of the U.S.
333 and Mexico (Figure 11). The largest increases are projected to occur in the Midwest and
334 northeast US, where ND>90F is projected to increase by 50% to 100% by the late 21st century
335 relative to its current climatology. An increase of ND>90F by 10%-50% is also projected over
336 the Southwest and South Central U.S., where ND>90F is climatologically high during the 20th
337 century. These models also consistently project a weak increase of ND>90F over Wyoming,
338 Utah and Colorado. Generally, the models that underestimate climatological ND>90F (Figure
339 11) tend to project a weaker increase of ND>90F (e.g., MPI, IPSL, MRI), whereas models that
340 overestimate climatological ND>90F tend to project a stronger increase of ND>90F (e.g.,
341 HadGEM2, MIROC5). These discrepancies are greatest near the Pacific Coast. The CCSM4 has
342 the least bias and projects an increase of 50-100% of ND>90F over Midwest, Northeast and
343 Pacific Coast, and up to 50% over the Southwest and South Central U.S.
344 Under RCP8.5, except for MRI which severely underestimates historical ND>90F, all
345 other models project that ND>90F over the majority of the U.S. south of 40^{o}N will exceed 60-90
346 days. The spatial pattern of increasing ND>90F is generally similar to that projected under
347 RCP4.5, but with 10-30% greater magnitude.
348

349 **4. Regional Climate**

350 *a. North Pacific and North Atlantic Storm Tracks*

351 The projected change in Northern Hemisphere storm tracks has been examined based on
352 6-hourly data available for 16 models from the CMIP5 archive (Figure 12). Near the tropopause
353 (250 hPa), the models project a strengthening of the storm track (ST) on its poleward flank, and a
354 slight weakening on its equatorward flank during Northern Hemisphere winter. In summer, the
355 models project a significant decrease in upper tropospheric ST activity south of the ST peak, and
356 weak increase over the high latitudes. These results are consistent with previous studies based on
357 CMIP3 (e.g. Yin 2005; Teng et al 2008) that indicate a poleward shift of the STs under global
358 warming.

359 In the mid-troposphere (500 hPa), the models mainly project a decrease in ST activity.
360 Some indication exists that over the Central and Western Pacific, the decrease is largest on the
361 equatorward flank of the ST in winter, while over the Eastern Atlantic, the decrease is largest
362 again on the southern flank of the ST in summer, but the shift is not as clear as that found near
363 the tropopause level. Near the surface, the models project mainly a decrease in ST activity
364 extending from Alaska across Canada and the U.S., and extending into the Atlantic in winter,
365 with not much indication of a poleward shift. In summer, the maximum projected decrease is
366 found mainly on the equatorward flank of the ST, indicating weakening and poleward shift of the
367 ST. Projected changes from spring and fall lie between those for winter and summer, but results
368 from Spring (Fall) more resemble those from winter (summer).

369 Here we provide a complementary analysis to that above using the Hodges (1994; 1995)
370 cyclone-tracking scheme on 6-hourly mean sea level pressure data to assess changes in
371 extratropical cyclone activity along the East Coast. Sheffield et al. (2012a) presented the

historical (1979-2004) predictions of western Atlantic extratropical cyclones during the cool season (November to March) for the mean of 15 CMIP5 models, which shows substantial skill at simulating the distribution of cyclone activity, although with modest under prediction of amplitude. Colle et al. (2012) highlighted the details of this historical cyclone analysis and the 21st century predictions in this region using 15 CMIP5 models. Figures 13b-d shows the difference in cool season cyclone track density for the multimodel mean between each of the three separate 30-year future periods (2009-2038, 2038-2069, and 2069-2098) for RCP8.5 and the historical (1979-2004) period (Figure 13a). Only a slight decrease in cyclone activity is projected over parts the western Atlantic storm track for 2009-2038 (Fig. 13b); however, Colle et al. (2012) showed that this reduction may be more widespread if one only considers the highest resolution CMIP5 models. The reduction in cyclone density is more apparent in the multimodel mean for the 2038-2069 period, with a reduction of 0.2 – 0.5 cyclones per cool season per 50,000 km^2 (5-15% change), primarily along the southern half of the western Atlantic cyclone storm track, which is near the Gulf Stream boundary. Meanwhile, a slight increase in cyclone density is projected to the north over parts of the northern New England and Nova Scotia, enhanced in the highest resolution models (not shown). These future changes relative to the historical period continue to increase in size and amplitude (10-20%) for the 2069-2098 period. The cyclone density also decreases around the Great Lakes and to the east of southern Greenland.

A gradual reduction in the maximum intensity of cyclones occurs within the dashed box region of Fig. 13a for the three future periods (Fig. 14); however, this reduction is delayed around 990 hPa during the first two 30-year periods. By 2069-2098, a 0.5 to 1.5 (5-10%) reduction in the number of cyclones is projected between the 960 and 1010 hPa pressure bins. In

394 contrast, Colle et al. (2012) showed a 5-10% increase in the number of 960-980 hPa cyclones
395 along the U.S. East coast (not shown).
396
397 *b. Northeast U.S. and Western Atlantic precipitation*
398 In Sheffield et al. (2012a), several CMIP models were evaluated to determine how well
399 they can simulate precipitation over the Northeast U.S. and western Atlantic during the historical
400 period (1979-2004) cool season (November-March). Figure 15 shows the mean CMIP
401 precipitation for this historical period, as well as the precipitation difference (in mm/season and
402 percent change) for the early 21st century (2009-2038) minus historical and late 21st (2069-
403 2098) minus historical for these same models. For the early 21st century (Fig. 15b), the largest
404 precipitation increase (80-150 mm) is from the southeast U.S. northeastward into the western
405 Atlantic in association with the mid-latitude storm track, while the largest percentage increase is
406 over eastern Canada (15-25%). As illustrated in Fig. 13b, a slight decrease in extratropical
407 cyclones occurs in this region, which suggests that the same or fewer storms will have more
408 precipitation. By the later 21st century (Fig. 15c), the precipitation change from the historical is
409 15-25%, while the largest change of 50-85% (40-100 mm/season) is around eastern Canada.
410 Over the Northeast U.S., the mean precipitation increases 25-35% by the later 21st century. Over
411 inland locations of the Northeast U.S. (Fig. 15d), the number of relatively light precipitation
412 events (< 10 mm/day) increases from 5-20%, with much of this change occurring by the early
413 21st century. The number of relatively heavy precipitation events (> 20 mm/day) over the
414 Northeast U.S. doubles by the early 21st century, and increases by 5-6 times by the later 21st
415 century. The results suggest that a potential exists for a dramatic increase in the number of

extreme rainfall events over the Northeast U.S. during the next 50 -75 years.

c. Western Water

Changes in snow are important in western regions because of the implications for water resources and winter tourism (see Section 4c). Figure 16 shows changes in April SWE over the western US from nine models for RCP8.5. April SWE is an indicator of total snow accumulation over the winter-time and the potential water resources availability for the coming year, which is especially important in California and the Colorado River basin. All models project a decrease in April SWE of up to 100mm in the central Rockies and Canadian Rockies. The spatial resolution of the models is generally too coarse to discern the details of the Sierra Nevada range on the California-Nevada border, but the models project a decrease in April SWE over this area. This broad decline is consistent with high-resolution hydrological changes using downscaled projections (Hayhoe et al., 2004). The decrease in SWE is driven by higher temperatures that increase the ratio of rainfall to snowfall (winter time precipitation is projected to remain the same or increase slightly. See Fig. 1) and increase melt efficiency, therefore moving the spring melt earlier in the season. Consequences from the shift in snowmelt timing may also because water rights can be month dependent (Hayhoe et al., 2004).

d. North American monsoon

We first concentrate on the core of the NA monsoon (NAM) region (23^{o}N-30^{o}N, 105^{o}W-110^{o}W) to assess projected behavior in the subset of models that best simulate the historical precipitation climatology in this region. In Sheffield et al. 2012a, the seasonal cycle in

438 precipitation of 21 CMIP5 models over the historical period (1979-2005) were evaluated to
439 identify models that have a reasonable representation of the seasonal cycle in precipitation over
440 the core NAM region. The results of this analysis indicate that eight of the 21 models have small
441 (lag=0) phase errors with respect to the observations. Unfortunately, only six of these eight
442 models provide precipitation data for RCP 4.5 from 2070-2100 at the time of this analysis.
443 The RMS of the future minus historical monthly rainfall climatology and the annual
444 mean rainfall differences are shown in Figure 17 for these six models. The results suggest that,
445 even for models that correctly capture the timing of the seasonal cycle of precipitation in the
446 region, large discrepancies exist in what these models project for the monthly mean magnitude
447 (range of 0.1 to 0.5 mm/day) and annual mean changes (range of -0.25 to 0.15 mm/day) in
448 precipitation for the monsoon region. In some cases the projections reflect model historical
449 period biases, for example in the CanESM2 (dry) and UKMO HadGEM2 (wet) models
450 (Sheffield et al. 2012a). For models with little or no historical bias (CNRM-CM5 and CSIRO-
451 Mk3-6-0), agreement is somewhat better and suggests little to moderate drying for the NAM
452 region, consistent with the continental scale drying shown in Figure 1.
453 While the analysis described above suggests that projecting annual mean changes over
454 the core monsoon region remains a challenge for global models, changes on a seasonal basis may
455 be more robust, as suggested in Figures 1 and 2. In Figure 18 the multi-model average monthly
456 precipitation from thirteen models in the CMIP5 database capture a northward migration of
457 precipitation in the NAM region (longitudes 102.5^{o} to 115^{o}W) during the warm season. The
458 models' historical precipitation (b) begins later and is weaker than the observed estimate (a).
459 Model projections from RCP8.5 are consistent with the CMIP3 results (see introduction) and

460 demonstrate reduced precipitation between 10°-25°N through the cold season extending into June
461 and July, and increased precipitation in September and October, although this tendency also
462 resembles the bias of the models in the historical simulations. These reductions in precipitation
463 between 10°N-25°N in June and July are consistent with reduced Mexico and Caribbean
464 precipitation in this latitude band seen in Figures 1 and 2 for JJA.
465
466 *e. Great Plains Low Level jet*
467 The Great Plains low level jet (LLJ) is a basic component of the warm season circulation
468 in NA that provides a moisture source for Great Plains precipitation. It emerges in April,
469 strengthens and peaks in June and July, and vanishes in late September (e.g. Sheffield et al.
470 2012a). Figure 19 reviews the ability of five climate models to capture the intensity and seasonal
471 cycle of meridional flow in the LLJ region. . As shown in Figure 19, the NCAR CCSM4,
472 MPI_ESM, and HadESM2-CC models are best able to capture the amplitude of the LLJ during
473 boreal summer, and vertical cross sections and horizontal maps of the jet verify this behavior
474 (not shown here). Figure 20 shows how the jet strength evolves for the NCAR CCSM4,
475 MPI_ESM, and HadESM2-CC models in RCP4.5 and RCP8.5. The projections generally
476 indicate a strengthening of the LLJ by about 15-25% in these three models by 2071-2100 in
477 RCP8.5.
478 The development of warm season precipitation anomalies or extreme wet and dry
479 conditions in the Great Plains and the Midwest is largely a result of the weather/precipitation
480 systems that develop and depend strongly on the dynamic stability of the large-scale circulation
481 (e.g., Moore et al. 2012; Veres and Hu 2012). This notion explains the apparent discrepancy

between the predicted strengthening LLJ shown in Fig. 20 and the decrease in summer precipitation in the Great Plains shown in Figures 1 and 2. This discrepancy suggests changes in the future summer circulation regime that would produce less precipitation in a moist environment with possibly a different intensity distribution of precipitation events in the Great Plains.

f. Arctic sea ice

Under RCP4.5 (Figure 21), the multi-model ensemble mean does not reach ice free-conditions by 2100, though the minus 1 standard deviation bound reaches nearly ice-free conditions (less than $1x10^6$ km^2) around 2050. In contrast, the multi-model mean ice extent drops below $1x10^6$ km^2 around 2060 for the RCP8.5 emission scenario, with the minus one standard deviation bound showing completely ice-free conditions by 2050. The September ice extent is stabilized around $4.0x10^6$ km^2 under RCP2.6 (not shown).

g. Warming hole in the Eastern U.S.

During the second half of the 20th century, the central-eastern U.S. experienced cooling trends while global mean temperatures warmed. We refer to this cooling region as a "warming hole" (WH), following Pan et al. (2004). A number of studies have attributed the mechanisms for this abnormal trend to large-scale decadal oscillations such as PDO and AMO (Robinson et al., 2002, Kunkel et al., 2006, Meehl et at., 2012). Other studies indicate that regional scale processes such as hydrological cycle (Pan et at, 2004) and land surface interaction (Liang et at. 2007) may play roles in the WH. Most CMIP3 models have had trouble reproducing the WH

504 (Kunkel et. al., 2006). In Sheffield et al. (2012b), it was shown that the 95% uncertainty range of
505 historical CMIP5 simulations does bracket the observed negative temperature trend, although the
506 multi-model mean time series had limited skill at reproducing the warming hole.

507 Here we assess whether any evidence for an eastern U.S. WH exists in 21st Century
508 projections. Figure 22 shows the multimodel mean DJF and JJA temperature trends during 2015-
509 2050 and 2051-2098 over NA for RCP8.5. The multi-model average in RCP8.5 shows relatively
510 slower warming in eastern U.S. compared to western U.S. during the winter (DJF), but little
511 signal in summer. Figures 23a and 23c show time series of 30 year running trends (warming rate)
512 of Eastern U.S. winter temperature for RCP8.5 and RCP4.5. The multimodel median of RCP8.5
513 simulations indicate a continued higher warming (~ 0.5 °C/decade) through the 21st cenutry,
514 whereas RCP4.5 indicates a decline in warming rate from ~ 0.4 °C/decade in the first half to ~
515 0.2°C/decade in the second half of the 21st Century (3rd panel), consistent with the stabilization
516 of forcing at 2050 in this pathway. Almost the entire uncertainty range in RCP 8.5, and the
517 majority of the uncertainty range in RCP 4.5, is above the zero line for 30 year running winter
518 temperature trend in eastern U.S. (Figure 23a,c); hence it is very likely in RCP 8.5, and likely in
519 RCP 4.5 that the negative temperature trend in eastern U.S. will disappear in the projected 21st
520 century climate.

521 Figure 23b and Figure 23d show the difference in trends between the east and west U.S. .
522 For the east – west temperature trend difference, the uncertainty range is equally distributed
523 above and below the zero line (Figures 23 b,d). A small negative difference (0.1°C) between east
524 and west temperature trends in Figure 22 could be the result of the selected time period. The
525 multi-model median curve in Figure 23b and Figure 23d varies between ±0.1°C. Hence, the

chance of relatively slower warming in the eastern U.S. compared to western U.S. is the same as the opposite

5. Tropical Intraseasonal Variability

a. Mid-summer drought

For most of Central America and southern Mexico, climatological precipitation is a maximum in June and September, bracketing a period of reduced rainfall during July-August known as the midsummer drought (MSD; Portig *et al.* 1961, Magaña *et al.* 1999). A previous assessment of CMIP3 model performance at simulating the MSD and future projections (Rauscher *et al.* 2008) suggested that many CMIP3 models are capable of simulating the MSD despite an overall dry bias, and that the MSD is projected to become stronger with an earlier onset. An updated evaluation of this feature (Sheffield et al. 2012b) indicates that many CMIP5 models are also able to capture both the spatial and temporal aspects of the MSD.

The CMIP5 multimodel mean projection for changes in precipitation during each of the summertime months (June through September) is shown in Figure 24. During each of the summertime months, the east Pacific ITCZ is projected to shift southward in concert with a drying over the east Pacific warm pool (EPWP), Central America/southern Mexico, and the Caribbean with enhanced drying over the major Caribbean islands of Cuba, Hispaniola, and Jamaica. The strongest drying is projected to occur during July and August, which are the months during which the MSD occurs in many regions throughout the Inter-Americas region. The precipitation changes shown are generally consistent with the JJA average precipitation patterns shown in Figure 1, although Western Mexico is projected to experience wetter

548 conditions during the late summer (September), consistent with the analysis of Figure 18.

549 Next, a simple algorithm for detecting and quantifying the climatological MSD strength
550 is used that does not assume a priori which months are maxima and which months constitute the
551 MSD (Karnauskas et al. 2012). Consistent with the month-by-month rainfall projections, the
552 CMIP5 multimodel mean provides a very robust projection of a stronger MSD for most regions
553 that experience an MSD today (Figure 25). The maximum MSD increases from ~2.5 mm/day to
554 ~3 mm/day (4 mm/day) in the RCP4.5 forcing experiment, and nearly doubles to >4 mm/day in
555 the RCP8.5 forcing experiment. The multimodel mean projection is qualitatively consistent in
556 each of the CMIP5 models that best replicate the observed MSD (Sheffield et al. 2012b). The
557 stronger MSD is a result of early and mid summer rainfall being reduced relative to the late
558 summer peak (see also Figure 18). The extension of the MSD northward along the Gulf coast of
559 Mexico and into the U.S. is projected to strengthen in both forcing experiments. Some regions
560 that did not previously exhibit a MSD (e.g., Panama) develop a moderate MSD under either
561 forcing experiments.

562

563 *b. Intraseasonal oscillation*

564 Some have argued that the leading mode of intraseasonal variability (ISV) in the east
565 Pacific warm pool is a regional manifestation of the Madden-Julian oscillation (Maloney et al.
566 2008). Sheffield et al. (2012b) documented the ability of CMIP5 models to capture this leading
567 mode of 30-90 day precipitation variability over the east Pacific and adjacent regions of Mexico
568 and Central America and the Caribbean during June-September. This analysis was done using
569 complex empirical orthogonal function (CEOF, Barnett 1983; Horel 1984) analysis that was

570 previously used to document the leading mode of ISV over the east Pacific during boreal
571 summer (Maloney et al. 2008). Based on a pattern correlation and assessment of amplitude of the
572 leading CEOF as compared to TRMM observations, seven models were judged to produce
573 realistic ISV.

574 Figure 26 shows the amplitude of the leading CEOF mode in one model with poor
575 simulation of ISV (CCSM4) and three models with realistic ISV (HadGEM2_CC,
576 HadGEM2_Es, MPI_ESM_LR) for 1981-2005, the 2076-2099 projection in RCP8.5, and the
577 difference in amplitude relative to present day. In the models with realistic ISV, robust changes
578 include increased amplitude of the leading CEOF on the southern fringe of the amplitude
579 maximum, with inconsistent changes in amplitude elsewhere. A plot of intraseasonal
580 precipitation variance supports these results (Jiang and Maloney 2012). Interestingly, some of
581 these models also exhibit significant decreases in ISV in the Caribbean. These changes in
582 variance mimic the mean precipitation changes shown in Figures 1 and 24.

583

584 **6. East Pacific and Atlantic Tropical Storm Track and Cyclone Activity**

585 *a. Tropical storm track*

586 The first approach we use to examine tropical storm activity is to calculate tropical storm
587 track statistics from 6-hourly 850 hPa relative vorticity following the method of Hodges (1995),
588 which captures traveling synoptic disturbances characteristic of the West Atlantic, Caribbean and
589 tropical East Pacific during summer (e.g. Serra et al. 2010). These systems contribute to the
590 majority of weather across the Intra-Americas Sea and are the seeds of a majority of West
591 Atlantic and East Pacific tropical cyclones. Figure 27 shows the 7-model mean for the future

592 period (May-November 2070-2100) and the future minus historical period differences in tropical
593 storm track density for each model. Several of these CMIP5 models (CanESM2, CCSM4,
594 HadGEM2-ES, MIROC5 and MRI-CGCM3) indicate a southward shift of the main storm track
595 as well as an increase in track density for the future projections, consistent with results found
596 using CMIP3 models (Bengtsson et al. 2006; Colbert et al. 2012). This southward shift is also
597 observed in the pattern of mean precipitation change seen in the JJA analysis in Figures 1 and 24.
598 No significant changes are observed in the mean strength of the tropical storm track based on
599 these seven models (not shown).
600
601 *b. Tropical Cyclones in the North Atlantic and Eastern North Pacific*
602 Using the Camargo and Zebiak (2002) algorithm we analyzed track changes in tropical
603 cyclone (TC)-like structures in RCP4.5 and RCP8.5 in four of the CMIP5 models shown by
604 Sheffield et al. 2012b to produce the best simulation of TC tracks in the current climate (GFDL-
605 ESM2M, MPI-ESM-LR, MRI-CGCM3, and MIROC5), although all of these models still
606 severely underestimate the number of TCs per year in the Atlantic and East Pacific.
607 Figure 28 shows the mean track density in the North Atlantic for the historical
608 simulations for the period 1951-2000, as well as the difference of the track density between the
609 period 2051-2100 and the historical track density for RCP4.5 and RCP8.5. While the MRI model
610 shows notable increases in TC track density for the Atlantic north of 25^{o}N, the MIROC model is
611 characterized by substantial decreases in this same region. Changes in the GFDL and MPI
612 models fall in between. To be more quantitative, Figure 29 shows the number of TCs in the
613 Atlantic and eastern north Pacific for these four models in the historical runs, and RCP4.5 and

614 RCP8.5. For the North Atlantic, the MRI model exhibits a significant increase in Atlantic TC
615 numbers in RCP8.5 relative to the historical period, whereas the MIROC5 model exhibits a
616 significant decrease in Atlantic TC numbers in both RCP4.5 and RCP8.5. For the East Pacific,
617 results are also mixed, with significant increases in TC numbers in future climate in the MPI
618 model in the RCP4.5 scenario, and significant decreases in the MIROC5 model.
619
620 *c. Downscaling with a high resolution model*
621 To complement the analysis in Section 5b, we use a dynamical downscaling approach in
622 which a high resolution global atmospheric model (GFDL HIRAM; Zhao et al. 2009; Zhao and
623 Held 2012) is integrated and forced by CMIP3 and CMIP5 coupled model projected SSTs and
624 sea ice concentrations. Recent studies suggest that when forced by the observed SSTs and sea-ice
625 concentrations, a global atmospheric model with a resolution ranging from 50km to 20km can
626 accurately simulate many aspects of TC/hurricane frequency and its variability for the past few
627 decades during which reliable observations are available (e.g., Sugi et al. 2002; McDonald et al.
628 2005; Yoshimura et al. 2006; Oouchi et al. 2006; Bengtsson et al. 2007; Gualdi et al. 2008;
629 LaRow et al. 2008; Zhao et al. 2009).
630 We first generate a present-day control simulation by prescribing climatological SSTs
631 and sea-ice concentration (seasonally varying with no interannual variability) using time-
632 averaged (1982-2005) Hadley Center Global Sea Ice and Sea Surface Temperature (HadISST)
633 data (Rayner et al. 2003). For the CMIP3 global warming experiments, we add the SST
634 anomalies (also seasonally varying with no interannual variability) projected by the coupled
635 models to the climatological SSTs and double the CO_2 concentration. For the CMIP5 high-

636 resolution time-slice simulations with prescribed SSTs and sea-ice concentrations, the
637 specifications for both the present-day and the future projection experiments also include
638 interannual variability, and feature future SSTs from two GFDL coupled models (ESM and
639 CM3). The results from downscaling the GFDL CMIP5 projections include changes in both
640 SST anomalies and different specifications for greenhouse-gases and aerosols depending on the
641 pathway used (Held et al 2012). The storm detection and tracking algorithm we use in the
642 analysis is described in (Zhao et al. 2009).

643 The GFDL C180HIRAM simulations with CMIP3 model forcing produce a large inter-
644 model spread (standard deviation of fractional changes ~ 0.35) in the N. Atlantic hurricane
645 frequency response to warming (Figure 30a). For example, the two Hadley Center models
646 produce the largest decrease while the ECHAM5 model generates a modest increase of
647 hurricanes. In contrast, the two GFDL CMIP5 models tend to produce an increase especially in
648 the near decade (2026-2035), and in the CM3 projections for RCP4.5. However, for RCP8.5,
649 both the CM3 and ESM produce insignificant change at the late 21st century.

650 Zhao and Held (2012) found that most of the inter-model spread in the N. Atlantic
651 hurricane frequency response among the CMIP3 models can be explained by a simple relative
652 SST (RSST) index defined as the tropical Atlantic SST minus tropical mean SST. Under global
653 warming scenarios the SST difference between the MDR and the other tropical ocean basins
654 varies from model to model with implications for hurricane activity (Latif et al. 2007; Swanson
655 2008; Vecchi et al. 2008; Wang and Lee 2008; Xie et al. 2010). The RCP4.5 projections for both
656 near decades and late 21st century from the CM3 and ESM models show consistent relationship
657 between the N. Atlantic hurricane frequency and the RSST (Figure 31a). However, the results

658 from the two late 21st century runs with RCP8.5 show a marked departure from the regression
659 line associated with the largest reduction (38% for CM3-2090-RCP8.5 and 25% for ESM-2090-
660 RCP8.5) in global mean hurricane frequency.. This departure is most likely a result of the larger
661 direct effect of the atmospheric greenhouses-gases concentration (RCP8.5) that can suppress
662 global and regional TC/hurricane frequency and therefore shift the hurricane frequency-RSST
663 regression line downward (Held and Zhao 2011). In general, the CMIP5 downscaling results
664 continue to suggest a large uncertainty in future projections of N. Atlantic hurricane frequency,
665 consistent with the analysis in Section 5a and 5b.
666 The GFDL CMIP5 downscaling results tend to produce a reduction in E. Pacific
667 hurricanes (Figure 30b, 31b). A negative correlation generally exists between the response of E.
668 Pacific and the N. Atlantic hurricane frequency. When the fractional changes are plotted against
669 the E. Pacific RSST index, we also see a strong correlation between E. Pacific hurricane
670 frequency and E. Pacific RSST. Again, the departure for the two RCP8.5 models at the late 21st
671 century supports that the global mean reduction due to the direct effect of GHG tends to
672 systematically move the regression line downward.
673
674 *d. Analysis of Atlantic wind shear and relative SST changes*
675 As discussed in Section 5c, at least to the middle of the 21st Century models indicate a
676 strong relationship between Atlantic hurricane activity and Atlantic RSST. Other studies suggest
677 the strong influence of Atlantic vertical shear (VS) variations in future climate on tropical
678 cyclone activity (e.g. Vecchi and Soden 2007). Here we assess the trends over the 21st Century in
679 Atlantic main development region (MDR; 85°W-15°W, 10°N-20°N) RSST and VS in CMIP5

680 models for RCP4.5. A broader set of CMIP5 models is used here than that used in Section 5c, so
681 as to obtain a more complete picture of shear and RSST changes across the ensemble. Recall that
682 RCP4.5 features a ramp up in radiative forcing to 4.5 W m^{-2} at 2050, and stabilization thereafter,
683 and hence the SST change and radiative forcing is more muted than that for the end of century
684 RCP8.5 time slice experiment discussed in Figure 31 where the RSST change becomes less
685 strongly related to Atlantic tropical cyclone activity.
686 A scatterplot of the MDR RSST and VS trends in the 21st century CMIP5 simulations is
687 shown in Fig. 32. The individual models show different responses of the MDR RSST and VS
688 trends, and hence suggest inconsistent changes in tropical cyclone activity, consistent with the
689 conclusions in Sections 5a-c. The linear fit of all models (the solid line in Fig. 32) shows that the
690 VS trend decreases with the MDR SST trend. This is consistent with a recent modeling study
691 (Lee et al. 2011), showing that a slower warming in the tropical North Atlantic compared with
692 the tropical Indo-Pacific Oceans increases the VS and static stability in the MDR for Atlantic
693 hurricanes.
694
695 **7. Interannual to Decadal Hydroclimate**

696 *a. Interannual variability*

697 The large internal variability of the El Niño/Southern Oscillation (ENSO) makes it
698 difficult to detect changes in ENSO properties over periods of a couple of centuries (Wittenberg
699 2009, Stevenson et al. 2012). Even without significant changes in ENSO itself, the long-term
700 trend in tropical SSTs and the associated changes in the midlatitude base state may result in

substantial changes in ENSO-related teleconnections (Meehl et al. 2006, Meehl and Teng 2007, Lau et al. 2008, Kumar et al. 2010, Stevenson et al. 2012). In this analysis, we evaluate whether the NA seasonal temperature and precipitation patterns associated with ENSO are projected to change significantly in the 21st century and beyond in CMIP5 models in RCP4.5 and RCP8.5. It should be noted that CMIP5 model performance in accurately simulating ENSO teleconnections in current climate is relatively poor (Sheffield et al. 2012b). We do not distinguish different types of ENSO episodes, such as CP from EP El Niño episodes that may change in proportion with climate change (Yeh et al. 2009), but rather consider a single broad class of ENSO events identified by the Niño3.4 SST index. We identify ENSO episodes in the same way as described in the historical analysis (Sheffield et al. 2012b).

On the basis of these calculations, we find that the frequency of ENSO episodes in the RCP4.5 and RCP8.5 simulations is approximately the same as in the historical simulations. A hint of increased ENSO amplitude exists, as the ensemble and episode mean peak Niño3.4 SST amplitude of El Niño episodes for the historical, RCP4.5, and RCP8.5 episodes is 1.42, 1.54, and 1.62°C, respectively; for La Niña episodes the mean peak amplitude is -1.32, -1.42, and -1.54°C, respectively. However, large inter-model variability exists, so these differences are not robust.

We calculate SAT and precipitation composites and assess significant differences in the same way as in the historical analysis and described in the Figure 33 caption (Sheffield et al. 2012b). Overall, we find that some models project significant changes in ENSO-related SAT and precipitation patterns, but most do not indicate significant changes in the 21st century. Moreover, because pattern changes vary from model to model, these changes are not robust in the ensemble mean. As an example, Figure 33 illustrates which models project significant SAT and

723 precipitation patterns in the winter of the mature ENSO episode [designated as DJF(0/1)]. The
724 two HadGEM2 models project significant SAT and precipitation pattern changes in the 21st
725 century, but most other models do not. For the models with simulations that extend beyond
726 2100, a tendency exists for significant changes from 2101-2300. In the ensemble calculations
727 (bottom row), however, all pattern changes are not statistically significant.
728
729 *b. Decadal variability*

730 Similar to our analysis for ENSO, we evaluate whether NA temperature and precipitation
731 patterns associated with the Pacific Decadal Oscillation (PDO) are projected to change in the
732 CMIP5 models. We define the PDO as the leading empirical orthogonal function of extended
733 winter (November-April) monthly mean sea surface temperature (SST) anomalies in the North
734 Pacific poleward of 20°N. We follow the same procedures for calculating SST anomalies,
735 performing the EOF analysis, and calculating the PDO index as described in the historical
736 analysis (Sheffield et al. 2012b), except that we now base the EOF analysis on the period from
737 2006-2090. Sheffield et al. (2012b) showed that CMIP5 models have success in reproducing the
738 PDO temperature teleconnection pattern, but mixed success at capturing the teleconnection
739 pattern in precipitation.
740 Overall, we find that SAT and precipitation pattern changes for individual models are
741 generally not significant, but some robust changes are apparent in the ensemble mean (Figure
742 34). The most notable change is found in spring (MAM) in the 21st century in RCP8.5 in
743 temperature. Most models do not project significant SAT or precipitation pattern changes in any
744 epoch, which probably relates to the limited sample size and the relative stability of the PDO-

745 related variability. However, in the ensemble mean of RCP8.5, where the sample size is
746 enhanced, the change of the 21st century SAT pattern is statistically significant at the 99% level.
747 Significant changes are also indicated in summer and fall of the 21st century, but as described
748 below, the magnitude of the statistically significant change is strongest in spring.

749 To determine the nature of the projected changes we show in Figure 35 the ensemble
750 mean MAM SAT regressions for the historical run and RCP8.5. Figure 35 indicates a clear
751 weakening of the PDO-related SAT variability in the warmer climate, with largest weakening
752 over western NA. We find that the PDO-related North Pacific SST variability does not show a
753 similar weakening, however. This finding suggests that increased ocean stratification, which
754 increases the SST response to a given a wind forcing, and/or the decrease in mean temperature
755 gradients may be responsible for the weakened PDO response. This weakening tendency is also
756 evident in summer and fall, but of weaker magnitude. Similar changes in winter also are
757 significant, but only after 2100.

758

759 **8. Conclusions**

760 We have examined 21st Century projections of NA climate in CMIP5 models under the
761 RCP4.5 and RCP8.5. In terms of robust projected changes, models indicate that warming will
762 occur everywhere in NA, with the greatest warming occurring in northern Canada where
763 multimodel mean temperature increases of 15^{o}C can be found during boreal winter in RCP8.5 at
764 the end of the 21st Century. It is very likely that the negative temperature trend (warming hole)
765 in the eastern U.S will disappear in the 21st Century. Models agree that more precipitation will

766 fall north of 40 degrees in winter, with the largest increases along the West coast and northeast
767 U.S. and Canada. The potential exists for a large increase in the number of extreme rainfall
768 events over the Northeast U.S., since many of the CMIP5 models for RCP8.5 suggest a 5-6 fold
769 increase in increase heavy precipitation events by the late 21st century. Model agreement is good
770 on reduced summertime precipitation in the Caribbean and Southern Mexico. Projected
771 precipitation increases are robust across models for Alaska and the Arctic rim during boreal
772 summer.

773 Further robust projected changes include a decrease in snow water equivalent throughout
774 the year, with the greatest decreases in January-April. Especially large decreases are noted in the
775 Rockies and Northwest Canada. The growing season is projected to lengthen across NA by the
776 end of the 21st Century, with the largest changes in western U.S. and Northern Mexico where
777 increases of two months or more are anticipated. In the agriculturally important regions of the
778 central U. S. and Canada, increases of 3-6 weeks are projected. Frost days are projected to
779 decrease across NA. An increase in the frequency of extended wet periods is projected for the
780 Eastern U.S.. Warm temperature extremes are projected to increase across NA, with the number
781 of 90 degree days to increase in the Midwest and Northeast U.S. by 50-100% relative to the
782 current climatology. Models that can resolve the Great Plains low level jet in current climate
783 project an increase in strength of the jet in the 21st Century. A poleward shift of the Atlantic
784 storm track is evidenced in the upper troposphere during all seasons. During winter, a general
785 decrease of storm track activity, especially in the Southern half of the Atlantic storm track, is
786 projected. Models tend to agree on a drier early monsoon season (June and July) and wetter late
787 season (September and October), consistent with a robust strengthening of the midsummer

788 drought in in Central America and the greater Caribbean region. Where comparisons are done,
789 RCP4.5 changes are often a more muted version of RCP8.5 change. One exception is in
790 hurricane activity, where the direct effect of greenhouse gases on TC/hurricane frequency
791 appears to become increasingly important relative to other factors (such as RSST) in the RCP8.5
792 at the end of the 21st Century.

793 Although many projected changes in NA climate are robust across CMIP5 models,
794 substantial disagreement in some areas helps to define priorities for future research. The sign of
795 mean precipitation changes across the southern U.S. is inconsistent among models. Models
796 disagree on annual mean precipitation changes in the NA monsoon region. Models disagree on
797 snow water equivalent changes on a regional basis, especially in transitional regions where
798 competing effects occur due to greater snowfall and warming temperatures. In the southeastern
799 U.S., the multimodel mean diurnal temperature range (DTR) signal is rather weak, accompanied
800 by larger variance among the models. The western U.S. is characterized by large intermodel
801 variability in the number of frost days in the Western U.S., where multimodel mean decreases in
802 frost days (greater than 70 days in RCP8.5) are also largest. Models do not agree on how
803 intraseasonal variability will change over the Caribbean and Gulf of Mexico, which may have
804 implications for future modulation of hurricane activity. Projected changes in seasonal mean
805 Atlantic and east Pacific tropical cyclone activity are inconsistent among models, which disagree
806 on the sign and amplitude of changes in environmental factors that modulate hurricane activity.
807 Models are highly inconsistent in projecting how the ENSO teleconnection to NA will change.

808 Model success in simulating historical climate as shown in Parts 1 and 2 of this study
809 (Sheffield et al. 2012a,b) lend confidence to many of the projected results. However, model

biases in other areas decrease confidence in projections, including changes of the timing of NA monsoon precipitation that exhibits projected changes in the same sense as historical biases. Growing season length is projected to increase most strongly over along the West Coast, where models tend to display large negative biases in historical runs. Models have substantial difficulties in simulating the historical distribution of persistent drought and wet spells, which produces less confidence in the pattern of extreme precipitation event changes in future climate.

This study represents an initial effort by the NOAA MAPP CMIP5 Task Force to provide an assessment of projected NA climate change over the 21st Century, although the analysis here just touches on what is available in the CMIP5 archive. More in-depth analysis of NA climate change is contained elsewhere in this special collection, and analysis of NA climate change in the CMIP5 archive will be expanded in years to come.

Acknowledgements: We acknowledge the World Climate Research Programme's Working Group on Coupled Modeling, which is responsible for CMIP, and we thank the climate modeling groups (listed in Table 1 of this paper) for producing and making available their model output. For CMIP the U.S. Department of Energy's Program for Climate Model Diagnosis and Intercomparison provides coordinating support and led development of software infrastructure in partnership with the Global Organization for Earth System Science Portals. The authors acknowledge the support of NOAA Climate Program Office Modeling, Analysis, Predictions and Projections (MAPP) Program as part of the CMIP5 Task Force.

References

Arora, V. K., J. F. Scinocca, G. J. Boer, J. R. Christian, K. L. Denman, G. M. Flato, V. V. Kharin, W. G. Lee, and W. J. Merryfield, 2011: Carbon emission limits required to satisfy future representative concentration pathways of greenhouse gases, *Geophys. Res. Lett.*, **38**, L05805, doi:10.1029/2010GL046270.

Bao, Q., and others: The Flexible Global Ocean-Atmosphere-Land System model Version: FGOALS-s2. *Adv. Atmos. Sci*., submitted.

Barnett, T. P., 1983: Interaction of the monsoon and Pacific trade wind system at interannual time scales. Part I: The equatorial zone. *Mon. Wea. Rev.*, **111,** 756–773.

Bengtsson, L., K. I. Hodges, and E. Roeckner, 2006: Storm Tracks and Climate Change. *J. Climate*, **19**, 3518–3543.

Bengtsson, L., K. Hodges, M. Esch, N. Keenlyside, L. Kornblueh, J.-J. Luo, and T. Yamagata, 2007: How may tropical cyclones change in a warmer climate. *Tellus*, **59A**, 539–561.

Benjamini, Y., and Y. Hochberg, 1995: Controlling the false discovery rate: A practical and powerful approach to multiple testing. *J. Roy. Stat. Soc.*, **B57**, 289-300.

Bi, D., M. Dix, S. Marsland, T. Hirst, S. O'Farrell and coauthors, 2012: ACCESS: The Australian Coupled Climate Model for IPCC AR5 and CMIP5. AMOS conference, 2012 , Sydney, Australia (available online at https://wiki.csiro.au/confluence/display/ACCESS/ACCESS+Publications)

Biasutti M, and Sobel A.H., 2009: Delayed Sahel rainfall and global seasonal cycle in a warmer climate. *Geophys Res Lett.,* **36**. doi:10.1029/2009GL041303

Biasutti, M., A. H. Sobel, S. J. Camargo, and T. T. Creyts, 2012: Projected changes in the

physical climate of the Gulf Coast and Caribbean. **112**, 819-845.

Brown, R. D., and P. W. Mote, 2009: The response of Northern Hemisphere snow cover to a changing climate. *J. Climate*, **22**, 2124-2145.

Camargo, S. J., and S. E. Zebiak, 2002: Improving the Detection and Tracking of Tropical Cyclones in Atmospheric General Circulation Models. *Wea. Forecasting*, **17**, 1152–1162.

Christiansen, D. E., S. L. Markstrom, and L. E. Hay, 2011: Impacts of climate change on the growing season in the United States. *Earth Interactions*, **15**, Paper No 33.

Chylek, P., J. Li, M. K. Dubey, M. Wang, and G. Lesins, 2011: Observed and model simulated 20th Century Arctic temperature variability: Canadian Earth System Model CanESM2. *Atmospheric Chemistry and Physics Discussions*, **11** (8), 22,893–22,907, doi: 10.5194/acpd-11-22893-2011.

Colbert, A. J., B. J. Soden, G. A. Vecchi and B. P. Kirtman, 2012: Impact of climate change on North Atlantic tropical cyclone tracks. J. Climate (submitted).

Colle, B.A., Z. Zhang, K. Lombardo, P. Liu, E. Chang, M. Zhang, and S. Hameed, 2012: Historical and future changes in eastern North America and western Atlantic extratropical cyclones in the CMIP5 models during the cool season. Submitted to the *J. Climate.*

Collins M., S. F.B. Tett, and C. Cooper, 2001: The internal climate variability of a HadCM3, a version of the Hadley Centre coupled model without flux adjustments. *Clim Dyn.,* **17**, 61–81. doi:10.1007/s003820000094

Dai, A., K. E. Trenberth, and T. R. Karl, 1999: Effects of Clouds, Soil Moisture, Precipitation, and Water Vapor on Diurnal Temperature Range. J. Climate, 12, 2451–2473, doi: 10.1175/1520-0442(1999)0122.0.CO;2.

874 Das, T., M. D. Dettinger, D. R. Cayan, and H. G. Hidalgo, 2011: Potential increase in floods in
875 California's Sierra Nevada under future climate projections. *Climatic Change*, **109**, 71-
876 94.
877 Diffenbaugh, N. S., J. S. Pal, R. J. Trapp, and F. Giorgi, 2005: Fine-scaleprocesses regulate the
878 response of extreme events to global climate change, *Proc. Natl. Acad. Sci. USA*, **102**,
879 15,774– 15,778.
880 Diffenbaugh, N. S., and M. Scherer, 2011: Observational and model evidence of global
881 emergence of permanent, unprecedented heat in the 20th and 21st Centuries. *Climatic*
882 *Change*, **107**, 615-624.
883 Donner, L. J., with 28 co-authors, 2011: The dynamical core, physical parameterizations, and
884 basic simulation characteristics of the atmospheric component AM3 of the GFDL Global
885 Coupled Model CM3. *J. Climate*, **24**, doi:10.1175/2011JCLI3955.1.
886 Duffy, P. B., and C. Tebaldi, 2012: Increasing prevalence of extreme summer temperatures in the
887 U.S., **111**, 487-495.
888 Dufresne, J-L., and 58 co-authors, N, 2012: Climate change projections using the IPSL-CM5
889 Earth System Model: from CMIP3 to CMIP5, *Clim. Dyn.*, submitted.
890 Easterling, D.R., B. Horton, P. D. Jones, T. C. Peterson, T. R. Karl, D. E. Parker, M. J. Salinger,
891 V. Razuvayev, N. Plummer, P. Jamason and C. K. Folland, 1997: Maximum and
892 Minimum Temperature Trends for the Globe. *Science*, **277**, 364-367. DOI:
893 10.1126/science.277.5324.364.
894 Elsner, M. M., L. Cuo, N. Voisin, J. S. Deems, A. F. Hamlet, J. A. Vano, K. E. B. Mickelson, S.-
895 Y. Lee, and D. P. Lettenmaier, 2010: Implications of 21st Century climate change for the

hydrology of Washington state. *Climatic Change*, **102**, 225-260.

Francina, D., J. Canon, and J. Valdes, 2010: IPCC-AR4 climate simulations for the Southwestern US: the importance of future ENSO projections. *Climatic Change* , **99**, 499-514.

Frich, P., L. V. Alexander, P. Della-Marta, B. Gleason, M. Haylock, A. M. G. K. Tank, and T. Peterson: 2002, Observed coherent changes in climatic extremes during the second half of the twentieth century, *Clim. Res.,* **19**, 193-212.

Gent, P. R., and Coauthors, 2011: The Community Climate System Model Version 4. *J. Climate*, **24**, 4973–4991.

Gualdi, S., E. Scoccimarro, and A. Navarra, 2008: Changes in tropical cyclone activity due to global warming: results from a high-resolution coupled general circulation model. *J. Climate*, **21**, 5204–5228.

Gutzler, D. S., and T. O. Robbins, 2011: Climate variability and projected change in the western United States: Regional downscaling and drought statistics. *Climate Dyn*., **37**, 835-849.

Hamlet, A. F. and D. P. Lettenmaier, 2007: Effects of 20th century warming and climate variability on flood risk in the western U.S., *Water Resour. Res.*, **43**, W06427, doi:10.1029/2006WR00509

Hay, L. E., S. L. Markstrom, and C. Ward-Garrison, 2011: Watershed-scale response to climate change through the 21st century for selected basins across the United States. *Earth Interactions*, **15**, Paper No 17.

Hayhoe, K., and others, 2004: Emission pathways, climate change, and impacts on California. *Proc. Nat. Acad. Sci*., **101**, 12422–12427.

Hazeleger, W., and 31 co-authors, 2010: EC-Earth: A seamless Earth system prediction approach

in action. *Bull. Amer. Meteor. Soc.*, **91**, 1357-1363, doi: 10.1175/2010BAMS2877.1

Held, I. and M. Zhao, 2011: The response of tropical cyclone statistics to an increase in CO2 with fixed sea surface temperatures. *J. Climate*, **24**, 5353–5364.

Held, I. M. and coauthors, 2012: High resolution AMIP simulation for CMIP5 using GFDL's HIRAM model. *J. Climate*, manuscript in preparation.

Hodges, K. I., 1994: A general method for tracking analysis and its application to meteorological data. *Mon. Wea. Rev.*, **122**, 2573–2586.

Hodges, K. I., 1995: Feature Tracking on the Unit Sphere. *Mon. Wea. Rev.*, **123**, 3458–3465.

Horel, J. D., 1984: Complex principal component analysis: Theory and examples. *J. Appl. Meteor.*, **23,** 1660–1673.

IPCC, 2007: Climate change 2007: I. The physical science basis. Cambridge University Press, London, 996pp.

Jiang, X.-A., E. D. Maloney, J.-L. F. Lin, and D. E. Waliser, 2012: Simulations of the east north Pacific intraseasonal variability in CMIP5 GCMs. *J. Climate*, submitted.

Jones, C. D., and others, 2011: The HadGEM2-ES implementation of CMIP5 centennial simulations, *Geosci. Model Dev.*, **4,** 543-570, doi:10.5194/gmd-4-543-2011.

Jungclaus J.H,. and others, 2006: Ocean circulation and tropical variability in the coupled model ECHAM5/MPI-OM. *J. Climate*, **19**, 3952-3972.

Karl, T. R., and Coauthors, 1993: A New Perspective on Recent Global Warming: Asymmetric Trends of Daily Maximum and Minimum Temperature. *Bull. Amer. Meteor. Soc.*, **74**, 1007–1023.

Karnauskas, K.B., A. Giannini, R. Seager, and A.J. Busalacchi (2012) A simple mechanism for

940 the climatological midsummer drought along the Pacific coast of Central America.
941 *Atmósfera*, in revision.
942 Kim, D., A. H. Sobel, A. D. Del Genio, Y. Chen, S. Camargo, M.-S. Yao, M. Kelley, and L.
943 Nazarenko, 2012: The tropical subseasonal variability simulated in the NASA GISS
944 general circulation model, *J. Clim.*, in press.
945 Knutson, T., and Coauthors, 2010: Tropical cyclones and climate change. *Nat. Geosci.*, **3**, 157–
946 163, doi:10.1038/ngeo779.
947 Kumar, A., B. Jha, and M. L'Heureux, 2010: Are tropical SST trends changing the global
948 teleconnection during La Niña? *Geophys. Res. Lett*., L12702,
949 doi.:10.1029/2010GL043394.
950 Kunkel, K.E., X.-Z. Liang, J. Zhu, Y. Lin, 2006: Can CGCMs simulate the Twentieth-Century
951 Warming Hole‖ in the Central United States? *J. Climate*, **19**, 4137-4153.
952 Latif, M., N. Keenlyside, and J. Bader, 2007: Tropical sea surface temperature, vertical wind
953 shear, and hurricane development. *Geophys. Res. Lett*., **34**, doi:10.1029/2006GL027969.
954 LaRow, T., Y.-K. Lim, D. Shin, E. Chassignet, and S. Cocke, 2008: Atlantic basin seasonal
955 hurricane simulations. *J. Climate*, **21**, 3191–3206.
956 Lau, N.-C., A. Leetma, and M. J. Nath, 2008: Interactions between the responses of North
957 American climate to El Niño-La Niña and to the secular warming trend in the Indian-
958 Western Pacific Oceans. *J. Climate,* **21**, 476-494.
959 Lawrence, D. M., and A. G. Slater, 2010: The contribution of snow condition trends to future
960 ground climate. *Clim. Dyn.*, **34** (7-8), 969-981.
961 Lee, S.-K., D. B. Enfield, and C. Wang, 2011: Future impact of differential inter-basin ocean

962 warming on Atlantic hurricanes. *J. Climate*, **24**, 1264-1275
963 Liang, X.-Z., J. Pan, J. Zhu, K. E. Kunkel, J. X. L.Wang, and A. Dai, 2006: J. Geophys. Res.,
964 **111**, D10108, doi:10.1029/2005JD006685.
965 McDonald, R., D. Bleaken, D. Creswell, V. Pope, and C. Senior, 2005: Tropical storms:
966 representation and diagnosis in climate models and the impact of climate change. *Clim.*
967 *Dyn*., **25**, 19–36.
968 Magaña, V., J.A. Amador, and S. Medina, 1999: The Midsummer Drought over Mexico and
969 Central America. *J. Climate*, **12**, 1577–1588.
970 Mahajan, S., G. R. North, R. Saravanan, and M. G. Genton, 2012: Statistical significance of
971 trends in monthly heavy precipitation over the U.S., *Climate Dyn*, **38**, 1375-1387.
972 Maloney, E. D., D. B. Chelton, S. K. Esbensen, 2008: Subseasonal SST Variability in the
973 Tropical Eastern North Pacific during Boreal Summer. *J. Climate*, **21**, 4149–4167.
974 McKee, T. B., N. J. Doesken, and J. Kleist, 1993: The relationship of drought frequency and
975 duration to time scales. Preprints, Eighth conf. on Applied Climatology. Anaheim CA,
976 AMS, 179-184.
977 McKee, T. B., N. J. Doesken, and J. Kleist, 1995: Drought monitoring with multiple time scales.
978 Preprints, Nineth conf. on Applied Climatology. Dallas TX, AMS, 233-236.
979 Meehl, G. A., and C. Tebaldi, 2004: More intense, more frequent and longer lasting heat waves
980 in the 21st Century. *Science*, **305**, 994-997.
981 Meehl, G. A., H. Teng, and G. Branstator, 2006: Future changes of El Niño in two global
982 coupled climate models. *Clim. Dyn.* **26**, 549-566.
983 Meehl, G. A., and H. Teng, 2007: Multi-model changes in El Niño teleconnections over North

America in a future warmer climate. *Clim. Dyn.* **29**, 779-790.

Meehl, G. A., J. M. Arblaster, and G. Branstator, 2012: Mechanisms contributing to the warming hole and the consequent U.S. east-west differential of heat extremes. *J. Climate*, in press.

Meinshausen, M., S. J. Smith, K. Calvin, J. S. Daniel and M. L. T. Kainuma, et al., 2011: The RCP greenhouse gas concentrations and their extensions from 1765 to 2300. *Climatic Change*, **109**, 213-241.

Mo, K. C. 2008: Model based drought indices over the United States. *J. Hydromet*. **9**, 1212-1230.

Moore, B. J., P. J. Neiman, F. M. Ralph, F. E. Barthold, 2012: Physical Processes Associated with Heavy Flooding Rainfall in Nashville, Tennessee, and Vicinity during 1–2 May 2010: The Role of an Atmospheric River and Mesoscale Convective Systems. *Mon. Wea. Rev.*, **140**, 358–378.

Neelin, J. D., B. Langenbrunner, J. E. Meyerson, A. Hall and N. Berg, 2012: California winter precipitation change under global warming in the Coupled Model Intercomparison Project 5 ensemble. *J. Climate*, submitted.

Neelin J.D., M. Munnich, H. Su, J. E. Meyerson, C. E. Holloway, 2006: Tropical drying trends in global warming models and observations. *Proceeding Nat. Acad. Sci.*, **103**, 6110–6115. doi:10.1073/pnas.0601798103

Oouchi, K., J. Yoshimura, H. Yoshimura, R. Mizuta, S. Kusunoki, and A. Noda, 2006: Tropical cyclone climatology in a global-warming climate as simulated in a 20 km mesh global atmospheric model: Frequency and wind intensity analysis. *J. Meteor. Soc. Japan*, **84**, 259–276.

1006 Pan, Z., R. W. Arritt, E. S. Takle, W. J. Gutowski Jr., C. J. Anderson, and M. Segal, 2004:
1007 Altered hydrologic feedback in a warming climate introduces a “warming hole”,
1008 *Geophys. Res. Lett.*, **31**, L17109, doi:10.1029/2004GL020528.
1009 Portig W. H., 1961: Some climatological data of Salvador, Central America. *Weather*, **16**, 103–
1010 112.
1011 Räisänen, J., 2008: Warmer climate: less or more snow? *Climate Dyn*., **30**, 307-319.
1012 Räisänen, J., L. Ruokolainen, and J. Ylhaisi., 2010: "Weighting of model results for improving
1013 best estimates of climate change." Climate Dynamics 35: 407-422.
1014 Rauscher, S. A., F. Giorgi, N. S. Diffenbaugh, and A. Seth, 2008: Extension and intensification
1015 of the meso-American mid-summer drought in the twenty-first century. *Climate Dyn*, **31**,
1016 551-571.
1017 Rayner, R., D. Parker, E. Horton, C. Folland, L. Alexander, and D. Rowel, 2003: Global analyses
1018 of sea surface temperature, sea ice, and night marine air temperature since the late
1019 nineteenth century. *J. Geophys. Res*., **108**, D14,4407,doi:10.1029/2002JD002 670.
1020 Robinson, W.A., R. Reudy and J.E. Hansen, 2002: General circulation model simulations of
1021 recent cooling in the east-central United States. *J. Geophys. Res*., **107,** D24, 4748,
1022 doi:10.1029/2001JD001577.
1023 Rotstayn, L. D., M. A. Collier, Y. Feng, H. B. Gordon, S. P. O’Farrell, I. N. Smith, and J.
1024 Syktus, 2010: Improved simulation of Australian climate and ENSO-related rainfall
1025 variability in a GCM with an interactive aerosol treatment, *Int. J. Climatol*., **30**, 1067–
1026 1088.
1027 Ruiz-Barradas, A., and S. Nigam, 2010: Great Plains Precipitation and Its SST Links in

1028 Twentieth-Century Climate Simulations, and Twenty-First- and Twenty-Second-Century
1029 Climate Projections. *J. Climate*, **23**, 6409–6429.
1030 Seager, R. and G. A. Vecchi, 2010: Greenhouse warming and the 21st century hydroclimate of
1031 southwestern North America. *Proc. Nat. Acad. Sciences,* **107**, 21277-21282.
1032 Seager, R., M. Ting, I. Held, Y. Kushnir, J. Lu, G. Vecchi, H.-P. Huang, N. Harnik, A. Leetmaa,
1033 N.-C. Lau, C. Li, J. Velez, and N. Naik, 2007: Model Projections of an Imminent
1034 Transition to a More Arid Climate in Southwestern North America. *Science*, **316**, 1181-
1035 1184.
1036 Serra, Y. L., G. N. Kiladis, and K. I. Hodges, 2010: Tracking and Mean Structure of Easterly
1037 Waves over the Intra-Americas Sea. *J. Climate*, **23**, 4823–4840.
1038 Seth, A., S. A. Rauscher, M. Rojas, A. Giannini, and S. J. Camargo, 2011: Enhanced spring
1039 convective barrier for monsoons in a warmer world? *Climatic Change*, **104**, 403-414.
1040 Seth A., M. Rojas, and S. A. Rauscher, 2010: CMIP3 projected changes in the annual cycle of
1041 the South American monsoon. *Climatic Change*, **98**, 331–357. doi:10.1007/s10584-009-
1042 9736-6
1043 Sheffield, J., and others, 2012a: North American Climate in CMIP5 Experiments. Part I:
1044 Evaluation of 20th Century Continental and Regional Climatology. *J. Climate*, submitted.
1045 Sheffield, J., and others, 2012b: North American Climate in CMIP5 Experiments. Part II:
1046 Evaluation of 20th Century Intra-seasonal to Decadal Variability. *J. Climate*, submitted.
1047 Sheffield, J., and E. F. Wood, 2008: Projected changes in drought occurrence under future global
1048 warming from multi-model, multi-scenario, IPCC AR4 simulations. *Climate Dyn*., **31**,
1049 79-105.

1050 Smith, T. M., R.W. Reynolds, T. C. Peterson, and J. Lawrimore, 2008: Improvements to
1051 NOAA's historical merged land-ocean surface temperature analysis (1880-2006). *J*
1052 *Clim.,* **21**, 2283-2296.
1053 Stevenson, S., B. Fox-Kemper, M. Jochum, R. Neale, C. Deser, and G. Meehl, 2012: Will there
1054 be a significant change to El Niño in the 21st century? *J. Climate* CCSM4 special issue,
1055 accepted. (doi:10.1175/JCLI-D-11-00252.1)
1056 Sugi, M., A. Noda, and N. Sato, 2002: Influence of the global warming 105 on tropical cyclone
1057 climatology: An experiment with the JMA global model. *J. Meteor. Soc. Japan*, **80**, 249–
1058 272.
1059 Swanson, K. L., 2008: Nonlocality of Atlantic tropical cyclone intensities. *Geochem. Geophys.*
1060 *Geosyst*., **9**, Q04V01. doi:10.1029/2007GC001844.
1061 Taylor, K. E., R. J. Stouffer, and G. A. Meehl, 2012: An Overview of CMIP5 and the
1062 Experiment Design. *Bull. Amer. Meteor. Soc.*, **93**, 485–498.
1063 Tebaldi, C., K. Hayhoe, J. M. Arblaster, and G. A. Meehl 2006: Going to the extremes. *Climatic*
1064 *Change*, **79**, 185-211.
1065 Teng, H., W. M. Washington, and G. A. Meehl, 2008: Interannual variations and future change
1066 of wintertime extratropical cyclone activity over North America in CCSM3. *Climate*
1067 *Dynamics*, **30**, 673-686
1068 Vecchi, G.A., and B.J. Soden, 2007: Increased Tropical Atlantic Wind Shear in Model
1069 Projections of Global Warming, *Geophys. Res. Lett*., 34, L08702,
1070 doi:10.1029/2006GL028905.
1071 Vecchi, G. A., K. Swanson, and B. Soden, 2008: Whither hurricane activity? *Science*, **322**, 687-

689.

Veres, M.C., and Q. Hu, 2012: AMO-forced regional processes affecting summertime precipitation variations in the central United States. *J. Climate* (in press).

Voldoire, A., and others, 2012: The CNRM-CM5.1 global climate model: Description and basic evaluation, Clim. Dyn., doi:10.1007/s00382-011-1259-y, in press.

Volodin, E.M., N.A. Diansky, and A.V. Gusev (2010). Simulating Present-Day Climate with the INMCM4.0 Coupled Model of the Atmospheric and Oceanic General Circulations. Izvestia, *Atmospheric and Oceanic Physics*, **46**, 414-431

Vose, R. S., D. R. Easterling, and B. Gleason (2005), Maximum and minimum temperature trends for the globe: An update through 2004, Geophys. Res. Lett., 32, L23822, doi:10.1029/2005GL024379.

Wallace, J. M., G.-H. Lim, M. L. Blackmon, 1988: Relationship between Cyclone Tracks, Anticyclone Tracks and Baroclinic Waveguides. *J. Atmos. Sci.*, **45**, 439–462.

Wang, G., 2005: Agricultural drought in a future climate: results from 15 global climate models participating in the IPCC 4th assessment. *Clim. Dyn*., **25**, 739–753.

Wang, C., and S.-K. Lee, 2008: Global warming and United States landfalling hurricanes. *Geophys. Res. Lett*., **35**, L02708. doi:10.1029/2007GL032396.

Watanabe, M., and Coauthors, 2010: Improved Climate Simulation by MIROC5: Mean States, Variability, and Climate Sensitivity. *J. Climate*, **23**, 6312–6335.

Watanabe, S., H., T., Sudo, K., Nagashima, T., Takemura, T., Okajima, H., Nozawa, T., Kawase, H., Abe, M., Yokohata, T., Ise, T., Sato, H., Kato, E., Takata, K., Emori, S., and Kawamiya, M.: MIROC-ESM 2011: model description and basic results of CMIP5-

1094 20c3m experiments, *Geosci. Model Dev.*, **4**, 845-872.
1095 Wehner, M., D. R. Easterling, J. H. Lawrimore, R.R. Heim, R. S. Vose, B. D. Santer, 2011:
1096 Projections of Future Drought in the Continental United States and Mexico. *J.*
1097 *Hydrometeor*, **12**, 1359–1377.
1098 Wilks, D. S., 2006: On "field significance" and the false discovery rate. *J. Appl. Meteorol.*
1099 *Climatol.*, **45**, 1181-1189.
1100 Wittenberg, A. T., 2009: Are historical records sufficient to constrain ENSO simulations?
1101 *Geophys. Res. Lett.*, **36**, L12702, doi:10.1029/2009GL038710.
1102 Xie, P., and P.A. Arkin, 1997: Global precipitation: A 17-year monthly analysis based on gauge
1103 observations, satellite estimates, and numerical model outputs. *Bull. Amer. Meteor. Soc*.,
1104 **78**, 2539 - 2558.
1105 Xie, S.-P., C. Deser, G.A. Vecchi, J. Ma, H. Teng, and A.T. Wittenberg, 2010: Global warming
1106 pattern formation: Sea surface temperature and rainfall. *J. Climate*, **23**, 966–986.
1107 Xin X., Wu T., Zhang J., 2012a: Introductions to the CMIP 5 simulations conducted by the BCC
1108 climate system model (in Chinese). *Advances in Climate Change Research.* submitted.
1109 Yeh, S. W., J. S. Kug, B. Dewitte, M. H. Kwon, B. P. Kirkman, and F. F. Jin, 2009: El Niño in a
1110 changing climate. *Nature*, **461**, 511-514, doi:10.1038/nature08316.
1111 Yin, J. H., 2005: A consistent poleward shift of the storm tracks in simulations of 21st Century
1112 climate. *Geophys. Res. Lett.*, **32**, L18701, doi:10.1029/2005GL023684.
1113 Yoshimura, J., M. Sugi, and A. Noda, 2006: Influence of greenhouse warming on tropical
1114 cyclone frequency. *J. Meteor. Soc. Japan*, **84**, 405–428.
1115 Yukimoto, S., et al., 2012: A new global climate model of the Meteorological Research Institute:

MRI-CGCM3—Model description and basic performance, *J. Meteorol. Soc. Jpn.*, **90a**, 23–64.

Zanchettin, D., A. Rubino, D. Matei, O. Bothe, and J.H. Jungclaus, 2012: Multidecadal-to-centennial SST variability in the MPI-ESM simulation ensemble for the last millennium. *Clim. Dyn.*, **39**, 419-444 doi:10.1007/s00382-012-1361-9.

Zhang, Z. S., Nisancioglu, K., Bentsen, M., Tjiputra, J., Bethke, I., Yan, Q., Risebrobakken, B., Andersson, C., and Jansen, E., 2012: Pre-industrial and mid-Pliocene simulations with NorESM-L, *Geosci. Model Dev.*, **5**, 523-533, doi:10.5194/gmd-5-523-2012.

Zhao, M., and I. M. Held, 2012: TC-Permitting GCM Simulations of Hurricane Frequency Response to Sea Surface Temperature Anomalies Projected for the Late-Twenty-First Century. *J. Climate*, **25**, 2995–3009.

Zhao, M., I. M. Held, S.-J. Lin, and G. A. Vecchi, 2009: Simulations of global hurricane climatology, interannual variability, and response to global warming using a 50km resolution GCM. *J. Climate*, **22**, 6653–6678.

1133 **Table 1.** CMIP5 models evaluated and their attributes.

Model	Center	Atmospheric Horizontal Resolution (lon. x lat.)	Number of model levels	Reference
ACCESS1-0	Commonwealth Scientific and Industrial Research Organization/Bureau of Meteorology, Australia	1.875 x 1.25	38	Bi et al. (2012)
BCC-CSM1.1	Beijing Climate Center, China Meteorological Administration, China	2.8 x 2.8	26	Xin et al. (2012)
CanCM4	Canadian Centre for Climate Modelling and Analysis, Canada	2.8 x 2.8	35	Chylek et al. (2011)
CanESM2	Canadian Center for Climate Modeling and Analysis, Canada	2.8 x 2.8	35	Arora et al. (2011)
CCSM4	National Center for Atmospheric Research, USA	1.25 x 1	26	Gent et al. (2011)
CNRM-CM5.1	National Centre for Meteorological Research, France	1.4 x 1.4	31	Voldoire et al. (2011)
CSIRO-MK3.6	Commonwealth Scientific and	1.8 x 1.8	18	Rotstayn et al.

	Industrial Research Organization/Queensland Climate Change Centre of Excellence, AUS			(2010)
EC-Earth	EC-Earth Consortium	1.125x1.12	62	Hazeleger et al. (2010)
FGOALS-S2.0	LASG, Institute of Atmospheric Physics, Chinese Academy of Sciences	2.8 x 1.6	26	Bao et al. (2012)
GFDL-CM3	NOAA Geophysical Fluid Dynamics Laboratory, USA	2.5 x 2.0	48	Donner et al. (2011)
GFDL-ESM2M	NOAA Geophysical Fluid Dynamics Laboratory, USA	2.5 x 2.0	24	Donner et al. (2011)
GISS-E2-R	NASA Goddard Institute for Space Studies, USA	2.5 x 2.0	40	Kim et al. (2012)
HadCM3	Met Office Hadley Centre, UK	3.75 x 2.5	19	Collins et al. (2001)
HADGEM2-CC	Met Office Hadley Centre, UK	1.8 x 1.25	60	Jones et al. (2011)

HADGEM2-ES	Met Office Hadley Centre, UK	1.8 x 1.25	60	Jones et al. (2011)
INMCM4	Institute for Numerical Mathematics, Russia	2 x 1.5	21	Volodin et al. (2010)
IPSL-CM5A-LR	Institut Pierre Simon Laplace, France	3.75 x 1.8	39	Dufresne et al. (2012)
IPSL-CM5A-MR	Institut Pierre Simon Laplace, France	2.5 x 1.25	39	Dufresne et al. (2012)
MIROC5	Atmosphere and Ocean Research Institute (The University of Tokyo), National Institute for Environmental Studies, and Japan Agency for Marine-Earth Science and Technology, Japan	1.4 x 1.4	40	Watanabe et al. (2010)
MIROC-ESM	Japan Agency for Marine-Earth Science and Technology, Atmosphere and Ocean Research Institute (The University of Tokyo), and National Institute for	2.8 x 2.8	80	Watanabe et al. (2011)

	Environmental Studies			
MIROC-ESM-CHEM	Japan Agency for Marine-Earth Science and Technology, Atmosphere and Ocean Research Institute, U. of Tokyo, and National Institute for Environmental Studies, Japan	2.8 x 2.8	80	Wantanbe et al. (2011)
MPI-ESM-LR	Max Planck Institute for Meteorology, Germany	1.9 x 1.9	47	Jungclaus et al. (2006); Zanchettin et al. (2012)
MRI-CGCM3	Meteorological Research Institute, Japan	1.1 x 1.1	48	Yukimoto et al. (2012)
NorESM1-M and NorESM1-ME	Norwegian Climate Center, Norway	2.5 x 1.9	26	Zhang et al. (2012)

1134

1135

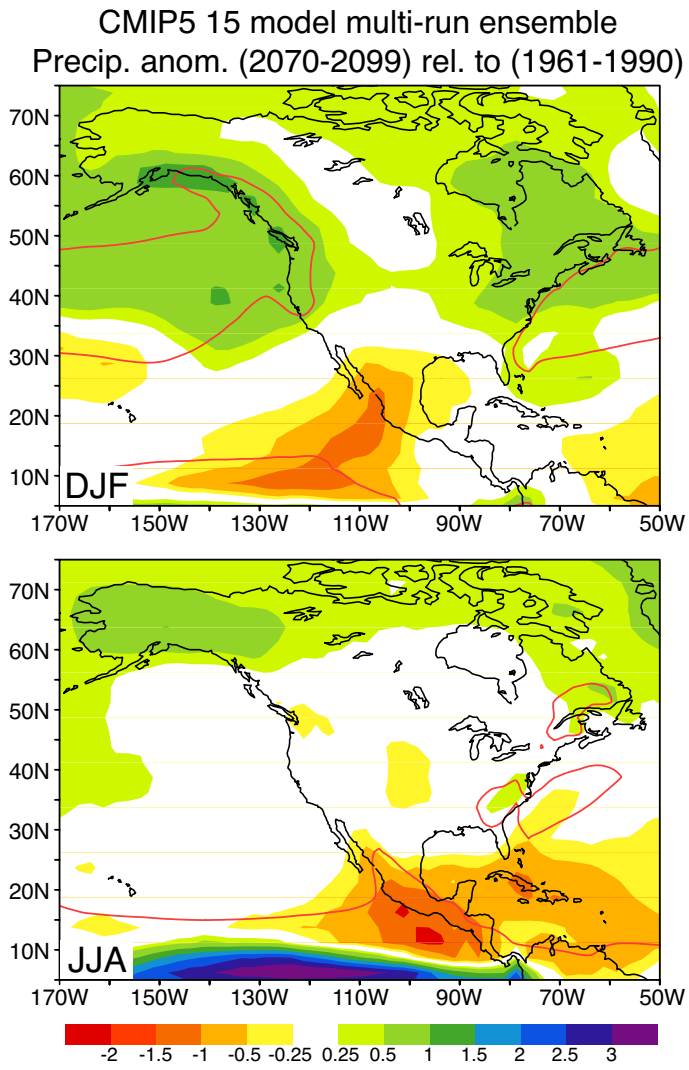

Figure 1. CMIP5 15 member multi-model, multi-run ensemble mean precipitation change for RCP8.5 for 2070-2099 relative to 1961-1990 base period for December-February (DJF) and June-August (JJA). Models used: BCC-ESM-1, CanESM2, CCSM4, CNRM-CM5, CSIRO, FGOALS-S2, GFDL-CM3, GISS-E2-R, HADGEM2-CC, INMCM4, IPSL-CM5A-MR, MIROC5, MPI-ESM-LR, MRI-CGCM3, NORESM1-M. Red line is the 4 mm/day 1961-1990 climatology. For models that have more than one run, the average is taken over runs prior to taking the multi-model mean.

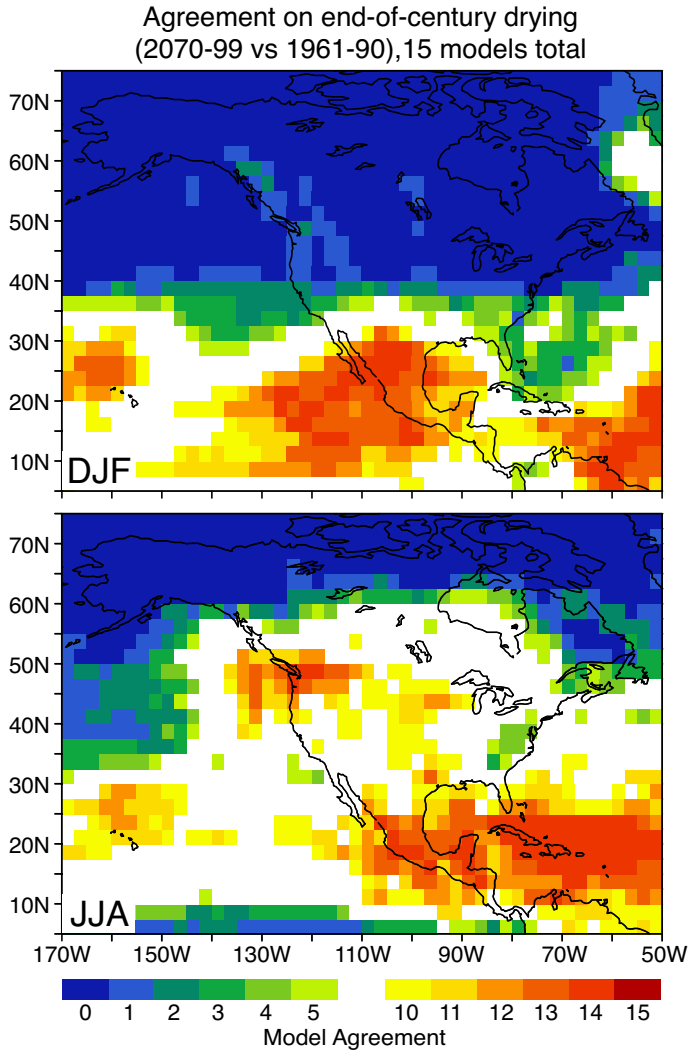

Figure 2. DJF and JJA plots of model agreement on sign of end-of-century precipitation change for the CMIP5 RCP8.5 scenario for the years 2070-2099, relative to a base period of 1961-1990. Red colors indicate a higher number of models (out of 15) that agree on a negative precipitation change; blue colors imply agreement on a positive precipitation change (shown as few models with negative change). Agreement is calculated on the sign of change alone; areas with fewer than 10 models agreeing on sign are unshaded.

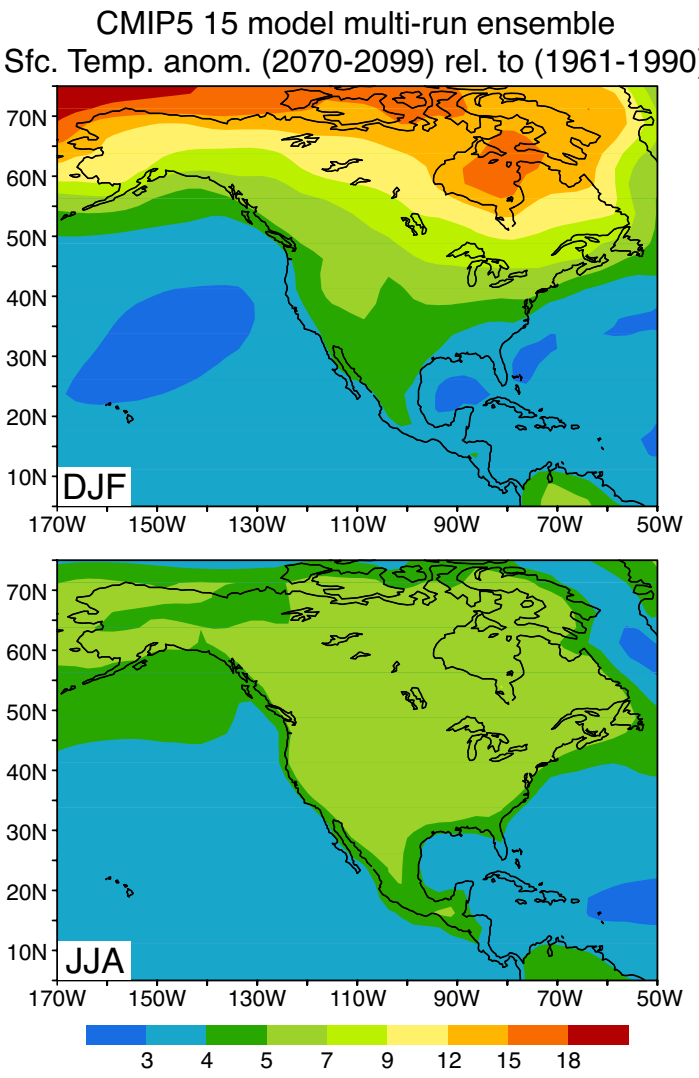

Figure 3. As in Figure 1, except for surface temperature change.

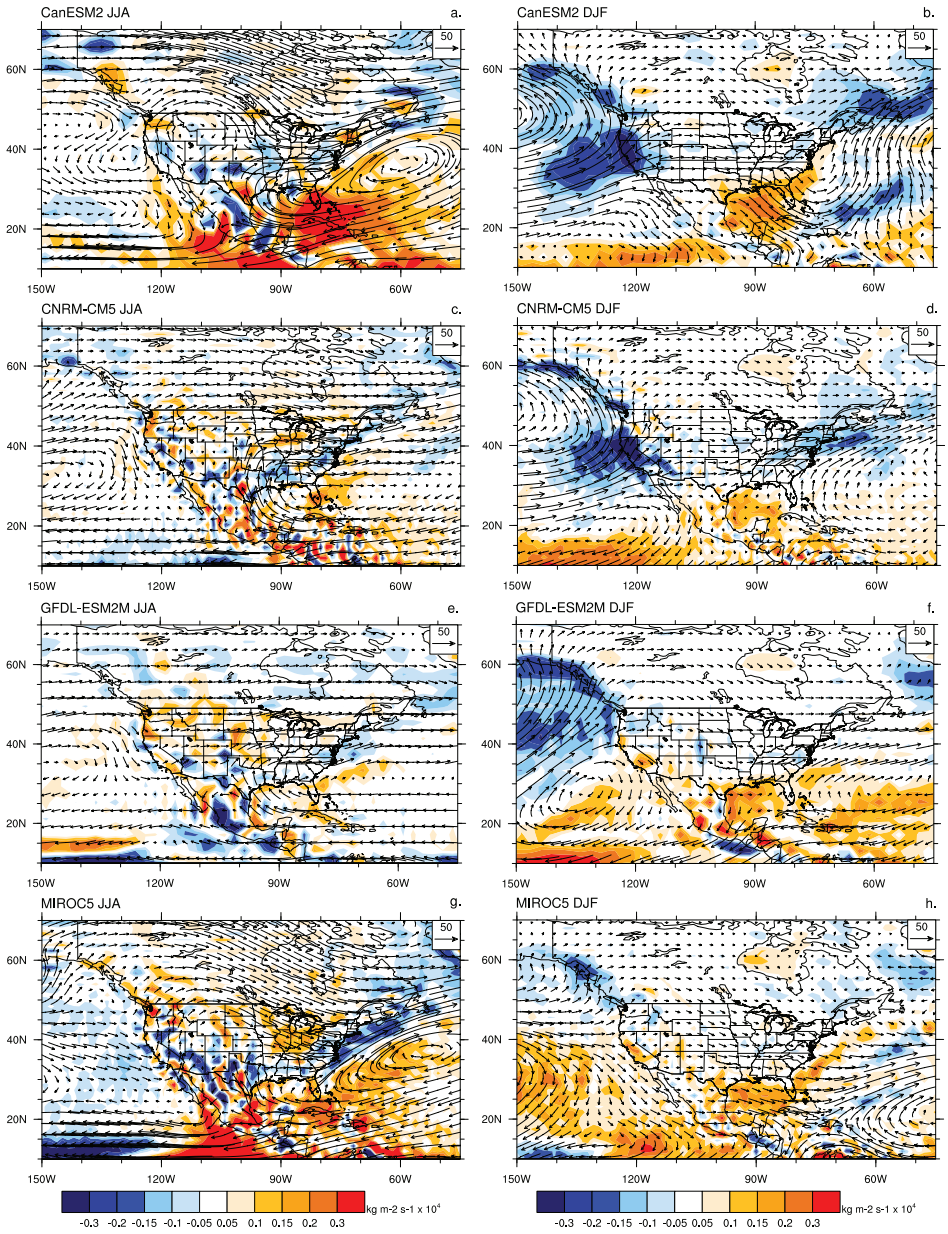

Figure 4. Mean JJA (left) and DJF (right) moisture transport integrated vertically to 500 hPa (VIMT shown as vectors, Kg/ms), and moisture divergence (color contours, $Kg/m^2s \times 10^4$) computed from four coupled models from CMIP5 (a-h) 2081-2100 minus 1981-2000 from the RCP8.5 and Historical experiments. The models used are CanESM2, CNRM-CM5, GFDL-ESM2M, and MIROC5, for which one realization of the required 6-hourly fields were available. This figure should be compared with the corresponding analysis from Sheffield et al. 2012a.

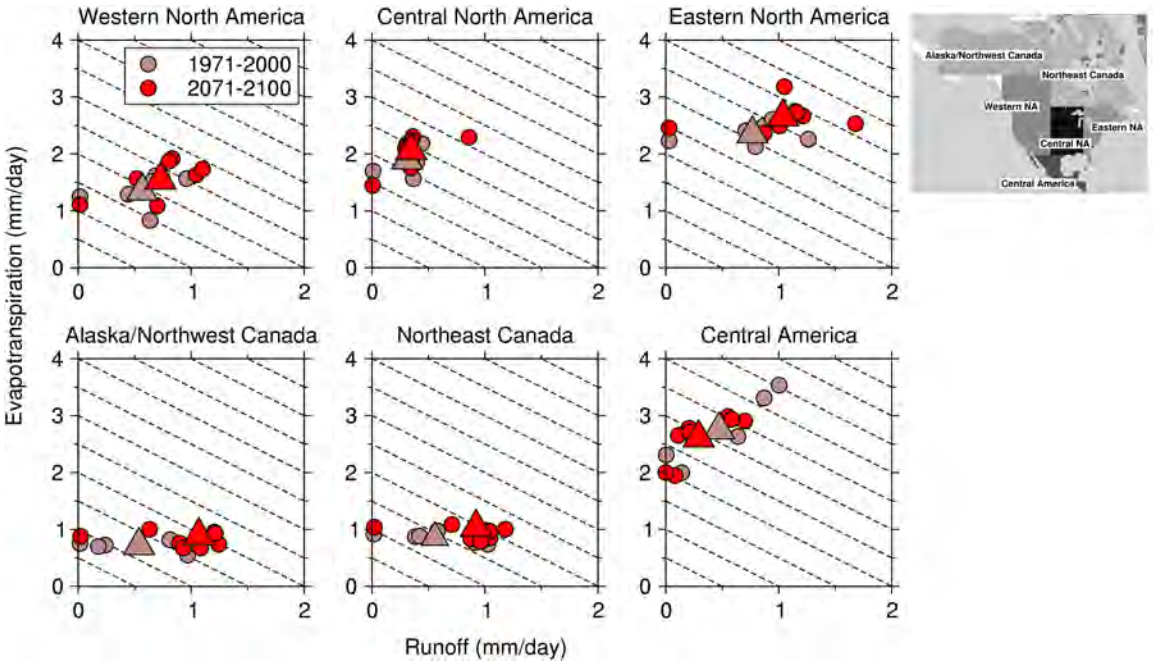

Figure 5. 30-year means from the historical (1971-2000) and RCP8.5 experiment (2071-2100) for regionally averaged runoff and evapotranspiration (mm/day). Six regions were defined for the North American continent: Central America, Western North America, Central North America, Eastern North America, Alaska/Northwest Canada, and Northeast Canada. The circles represent individual climate models. The large triangles represent the multi-model values. Precipitation balances runoff plus evapotranspiration over decadal time scales by assuming that there is no change in water storage. The diagonal lines represent contours of precipitation. A shift in the multi-model mean towards the upper-right indicates an increase in precipitation. A shift to the bottom-left indicates a decrease in precipitation. Values are calculated for 13 climate models (CanESM2, CSIRO-Mk3-6-0, GFDL-ESM2G, GISS-E2-H, GISS-E2-R, IPSL-CM5A-LR, IPSL-CM5A-MR, MIROC-ESM, MIROC-ESM-CHEM, MPI-ESM-LR, MRI-CGCM3, NorESM1-M, NorEMS1-ME) using one ensemble member each.

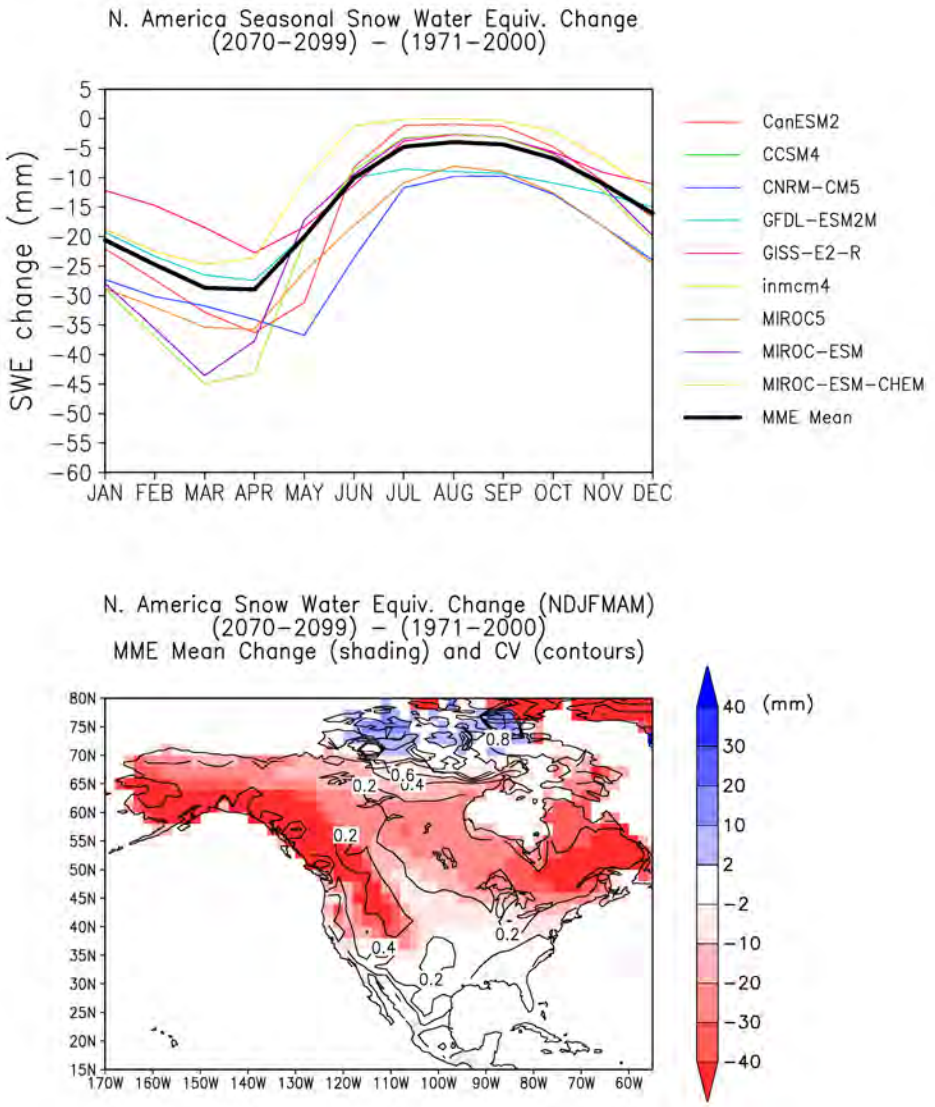

Figure 6. Changes in SWE (mm) from 9 CMIP5 models (one ensemble member each) from 1971-2000 to 2071-2100 for the RCP8.5 scenario. (top) Mean monthly change in SWE averaged over N. America (25N-80N, 170W-65W), and (bottom) spatial distribution of change in winter-spring (NDJFMAM) SWE (shading) and coefficient of variation (CV) of changes in SWE across models (contours). Some of the models have spuriously high snow accumulations at isolated grid cells and these are filtered out.

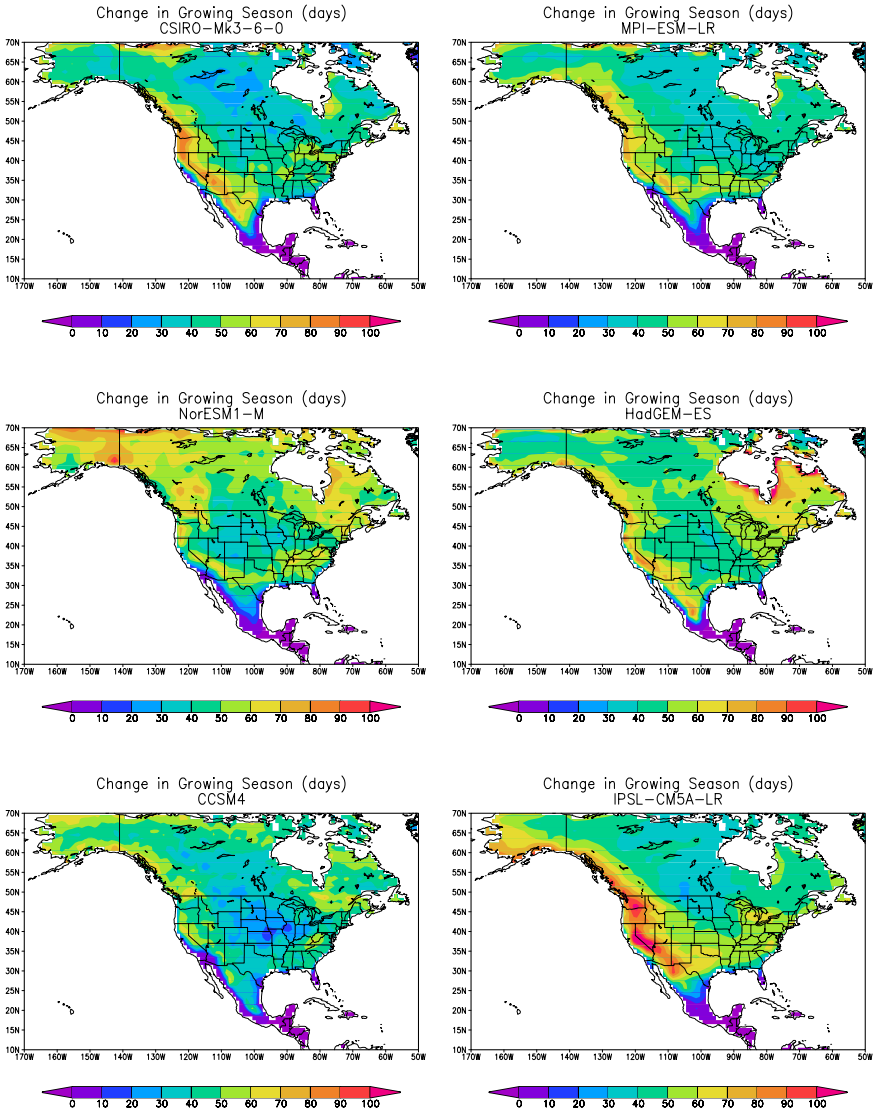

Figure 7. Projected changes in growing season length for 6 CMIP5 models (CCSM4, CSIRO-Mk-6-0, HadGEM-ES, IPSL-CM5A-LR, MPI-ESM-LR, NorESM1-M; all single ensemble member r1i1p1) for RCP8.5. Changes are calculated as the difference between the mean growing season length for 2071-2100 and 1971-2005. We define the growing season length following Schwartz et al. (2006), which is the number of days between the last spring freeze of the year and the first hard freeze of the autumn in the same year. A hard freeze is defined when the daily minimum temperature drops below -2°C. The end of century changes are calculated based on the change in 30-yr average growing season length (2071-2100 - 1971-2005).

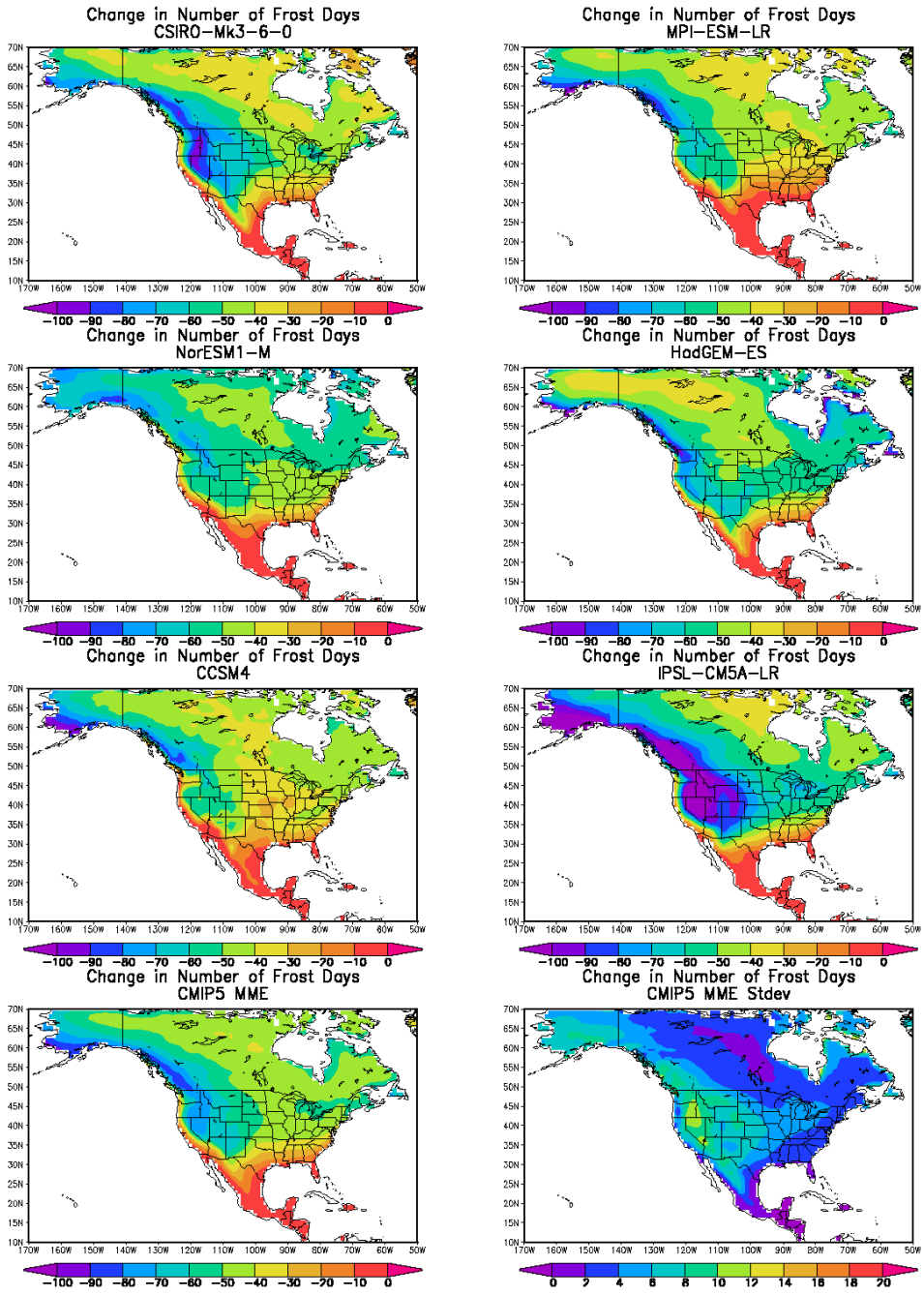

Figure 8. Change in the annual number of frost days (Tmin < 0°C) between 1979-2005 and 2071-2100 for the RCP8.5 scenario from six CMIP5 models (CSIRO-Mk3-6-0, MPI-ESM-LR, NorESM1-M, HadGEM-ES, CCSM4, IPSL-CM5A-LR). The first ensemble member is used for each model. Also shown are the MME mean change and the standard deviation of the change across the models. Frost days were calculated on the model grid and then the results interpolated to 2.0° resolution. Frost days are calculated as the annual number of days with T_{min} less than 0°C (Frick et al.,

2002) and then averaged over 1979-2005 for the "historical" and 2071-2100 for the RCP8.5 scenario.

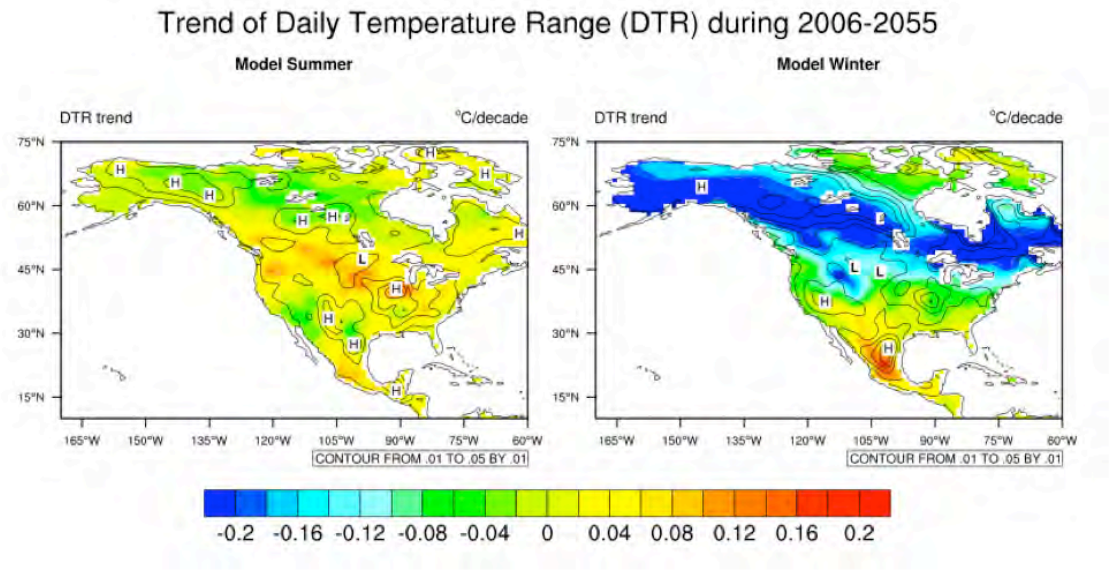

Figure 9. Trend of daily temperature range (T_{max} -T_{min}) during 2006-2055 averaged among 22 models with 63 members in the RCP45 experiment. The contours are the inter-model variance of the range.

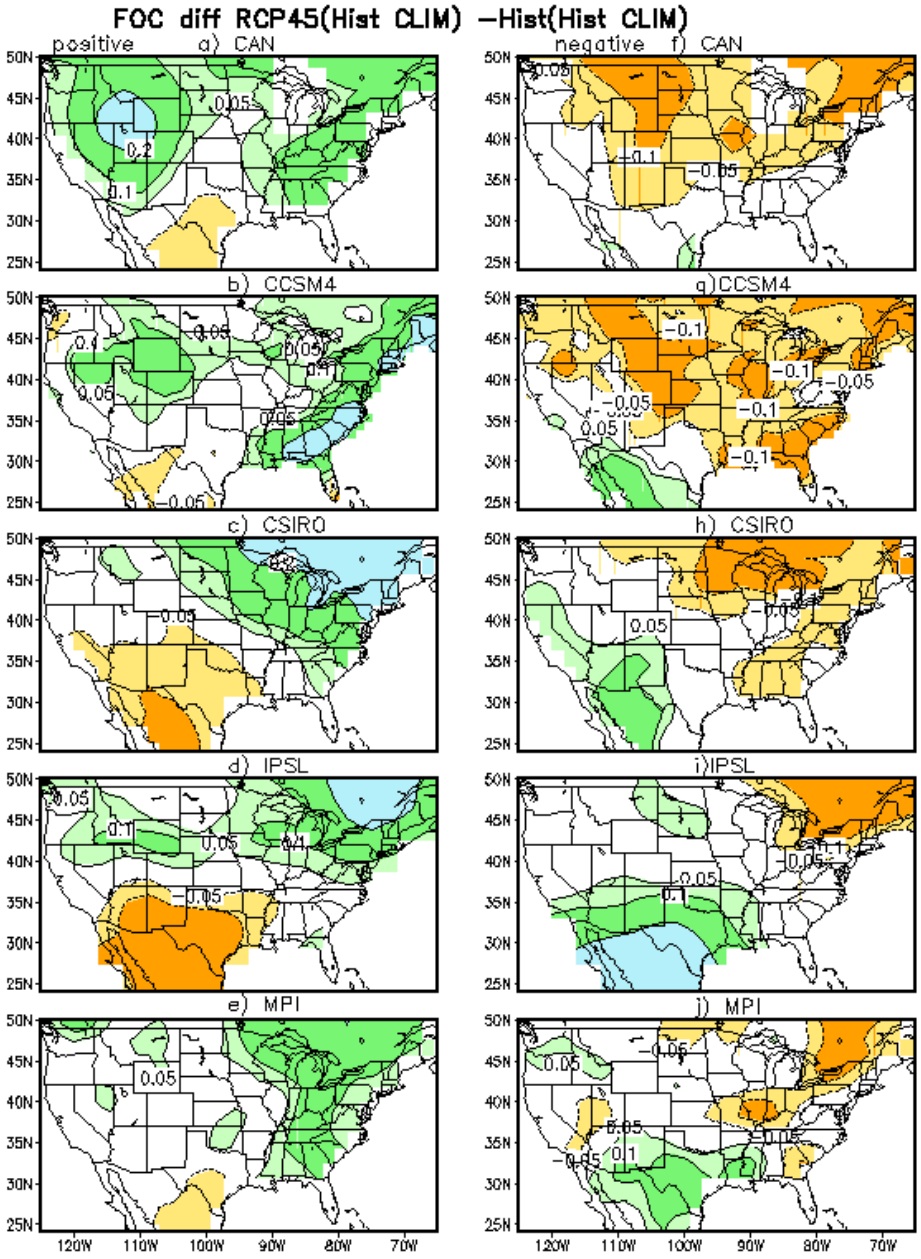

Figure 10. The difference in frequency of occurrence for RCP4.5 projection runs calculated using the RCP4.5 projected climatology minus historical runs calculated using the historical climatology defined by SPI6 averaged over positive (wet) events for (a) CAN, (b) CCSM4, (c) CSIRO, (d) IPSL, (e) MPI. (f)-(j) same as (a)-(e) but for negative (dry) events. Meteorological drought is measured by precipitation (P) deficit, and the index used to classify drought is the 6-month Standardized Precipitation Index (SPI6). Agricultural drought is measured by total soil moisture (SM), and the index used for drought classification is the SM percentiles [Mo 2008]. The SPI6 is computed by following the method outlined by Mckee et al. [1993, 1995]. The SM anomalies are normally distributed so SM percentiles are computed

based on a normal distribution function with parameters determined for each climate model. The Frequency of Occurrence (FOC) is the number of extreme events that last at least 9 months divided by the total number of events. An event is defined as extreme if the SPI6 reaches the threshold of +/- 0.8 or the SM percentile is above (below) 80%(20%).

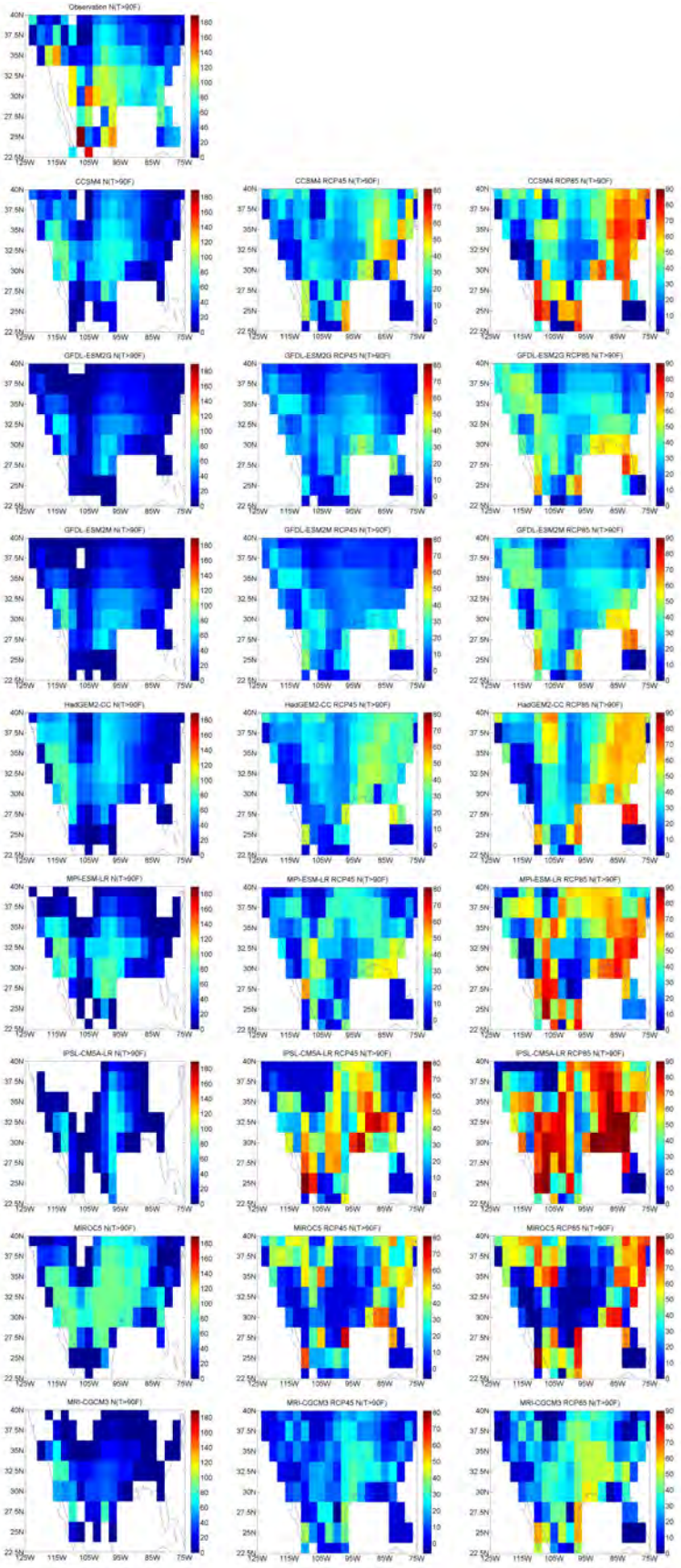
Observation N(T>90F)
CCSM4 N(T>90F)
CCSM4 RCP45 N(T>90F)
CCSM4 RCP85 N(T>90F)
GFDL-ESM2G N(T>90F)
GFDL-ESM2G RCP45 N(T>90F)
GFDL-ESM2G RCP85 N(T>90F)
GFDL-ESM2M N(T>90F)
GFDL-ESM2M RCP45 N(T>90F)
GFDL-ESM2M RCP85 N(T>90F)
HadGEM2-CC N(T>90F)
HadGEM2-CC RCP45 N(T>90F)
HadGEM2-CC RCP85 N(T>90F)
MPI-ESM-LR N(T>90F)
MPI-ESM-LR RCP45 N(T>90F)
MPI-ESM-LR RCP85 N(T>90F)
IPSL-CM5A-LR N(T>90F)
IPSL-CM5A-LR RCP45 N(T>90F)
IPSL-CM5A-LR RCP85 N(T>90F)
MIROC5 N(T>90F)
MIROC5 RCP45 N(T>90F)
MIROC5 RCP85 N(T>90F)
MRI-CGCM3 N(T>90F)
MRI-CGCM3 RCP45 N(T>90F)
MRI-CGCM3 RCP85 N(T>90F)

Figure 11. Climatological distribution of the number of days per year when temperature is greater than 90F over US and Mexico for the period of 1979-2005 derived from 9 CMIP5 models and Global Historical Climatology Network daily maximum surface temperature, as well as model projections for RCP4.5 and RCP8.5 for 2071-2100. T_{max} were mapped to a 2.5^{o}x2.5^{o} grid.

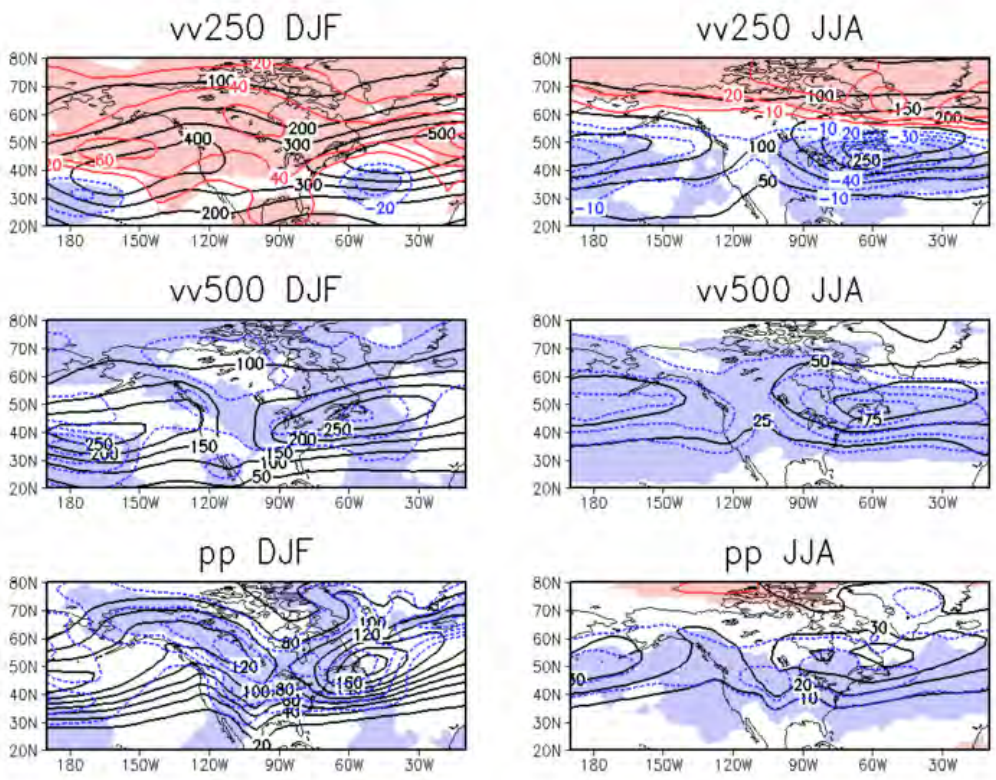

Figure 12. a) Solid contours: Winter (DJF) climatological (1980-1999) storm track activity, as indicated by variance of 24-hour difference bandpass filtered *v* at 250 hPa level, based on ensemble mean of 16 CMIP5 models (contour interval 100 m^2s^{-2}). The filter used is the 24-hour difference filter (Wallace et al. 1988), which highlights synoptic variability with periods of 1.2 to 6 days. The models examined are BCC-CSM1.1; CanESM2; CNRM-CM5; CSIRO-Mk3.6.0; GFDL-ESM2M; HadGEM2-CC; HadGEM2-ES; INM-CM4; IPSL-CM5A-LR; IPSL-CM5A-MR; MIROC5; MIROC-ESM; MIROC-ESM-CHEM; MPI-ESM-LR; MRI-CGCM3; and Nor-ESM1-M. Colored lines: Projected change (2081-2100 mean minus 1980-1999 mean) based on RCP8.5 (contour interval 20 m^2s^{-2}). Shades: grid boxes over which more than 80% of CMIP5 models agree on the sign of the projected change; b) Same as a), but for summer (JJA; contour intervals 50 m^2s^{-2} and 10 m^2s^{-2}); c) Same as a), but for 500 hPa level (contour intervals 50 m^2s^{-2} and 10 m^2s^{-2}); d) Same as c), but for JJA (contour intervals 25 m^2s^{-2} and 5 m^2s^{-2}); e) Same as a), but for variance of SLP (contour intervals 20 hPa^2 and 5 hPa^2); f) Same as e), but for JJA ((contour intervals 10 hPa^2 and 2.5 hPa^2).

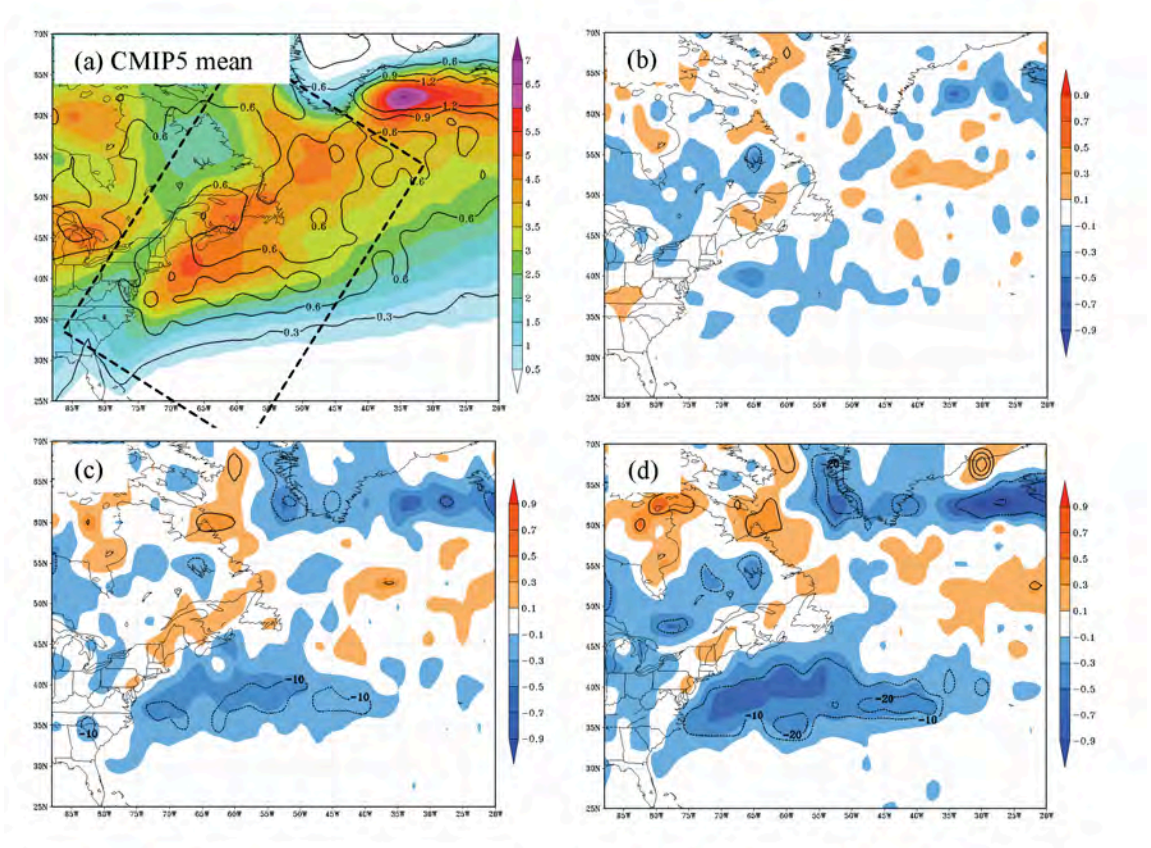

Figure 13. (a) Cyclone track density for the mean (shaded) and spread (contoured every 0.3) for 15 CMIP5 models (listed in Colle et al. 2012) showing the number of cyclones per cool season (November to March) per 50,000 km^2 for 1979-2004. Same as (a) except the difference in cyclone density (Future – historical) and percentage change between (b) 2009-2038, (c) 2038-2068, and (d) 2069-2098 and the historical 1979-2004 period. The models used to generate the ensemble mean include the CESM, EC-EARTH, MRI-CGCM3,CNRM-CM5,MIROC5,HadGEM2-ES, HadGEM2-CC, INMCM4, IPSL-CM5A-MR, MPI-ESM-LR, NorESM1, GFDL-ESM2M, IPSL-CM5A-LR, BCC-CSM1, and MIROC-ESM-C.

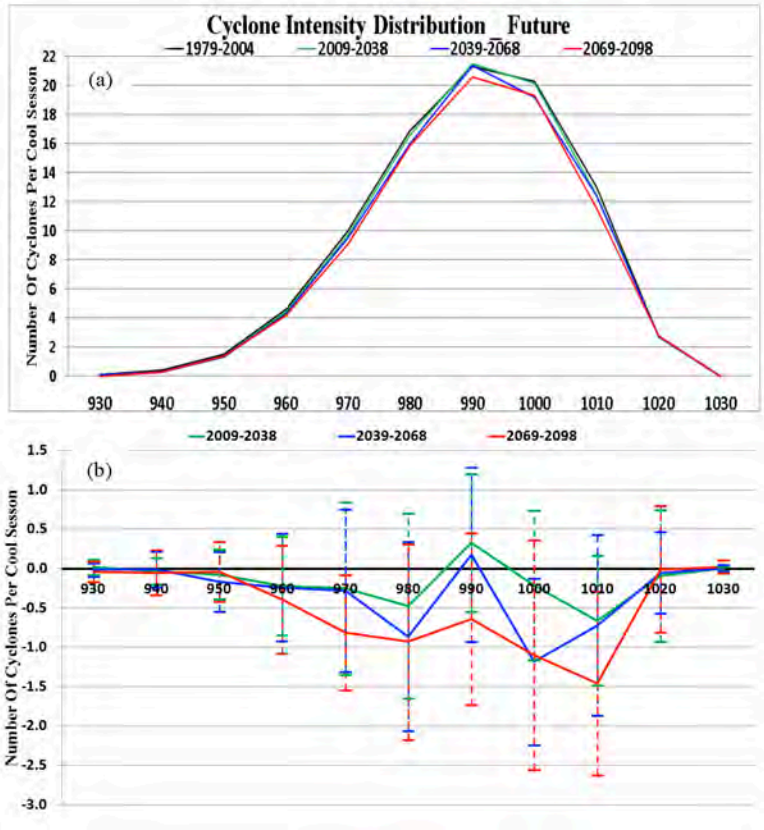

Figure 14. (a) Number of cyclone central pressures at their maximum intensity for the 1979-2004 cool seasons within the dashed box region in Fig. 14a for a 10 hPa range centered every 10 hPa showing the CMIP5 mean historical (black), (b) 2009-2038 (green), (c) 2038-2068 (black), and (d) 2068-2098 (red) years for the 15 CMIP5 models in Figure 14. (b) Same as (a) except the difference and standard deviation between three future periods and the historical 1979-2004 period.

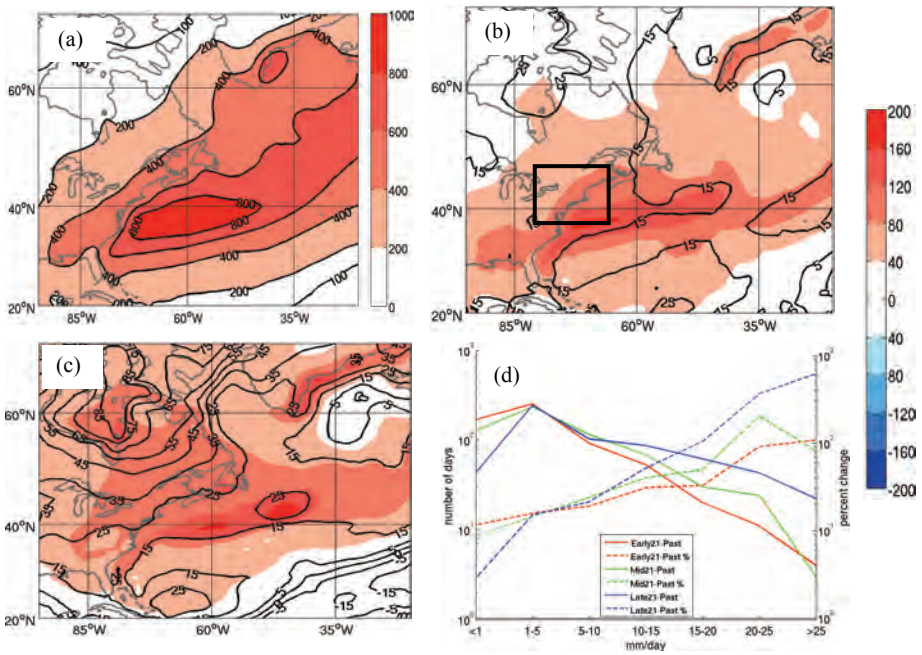

Figure 15. (a) Multimodel mean daily precipitation (mm/season) averaged for select CMIP5 members for the historical (1979-2004) period during the cool season (November – March). (b) Precipitation difference (shaded in mm/season) and the percentage change (solid every 10 percent) between the (b) 2009-2038 and the historical 1979-2004 period for the cool season (November – March). (c) Same as (b) except for the 2069-2098 period. (d) Difference in the number of precipitation days and percentage change for each amount bin between the 2009-2038, 2038-2068, and 2069-2098 and the historical 1979-2004 period for the land area only in the black box in (b). The models analyzed include BCC-CMS, GFDL-ESM2M, HadGEM2-CC,HadGEM2-ES, INMCM4, IPSL-CM5a, MIROC5-ESM, MICRO5, and NorESM.

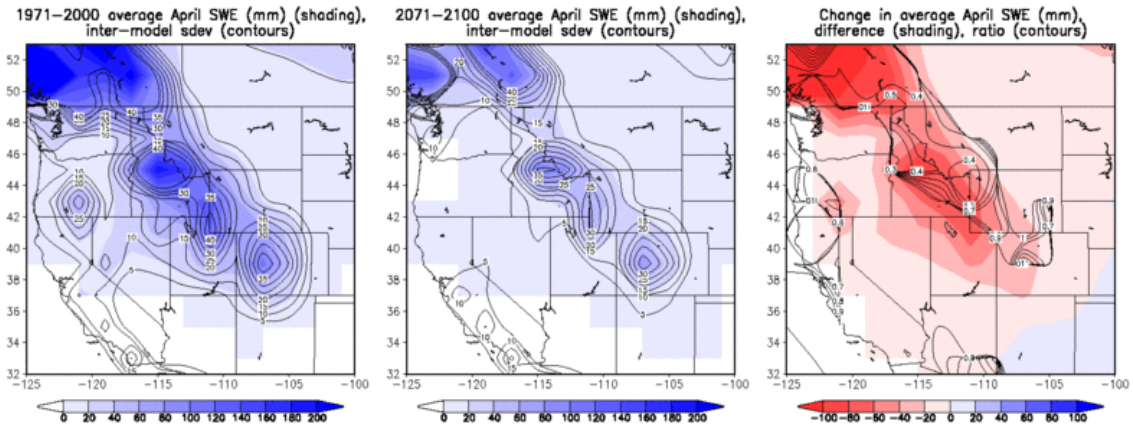

Figure 16. Average April SWE (mm) from 9 CMIP5 models for (a) 1971-2000, (b) 2071-2100 (RCP85) and (c) their difference and ratio. The models are: CanESM2, CCSM4, CNRM-CM5, GFDL-ESM2M, GISS-E2-R, inmcm4, MIROC5, MIROC-ESM, MIROC-ESM-CHEM.

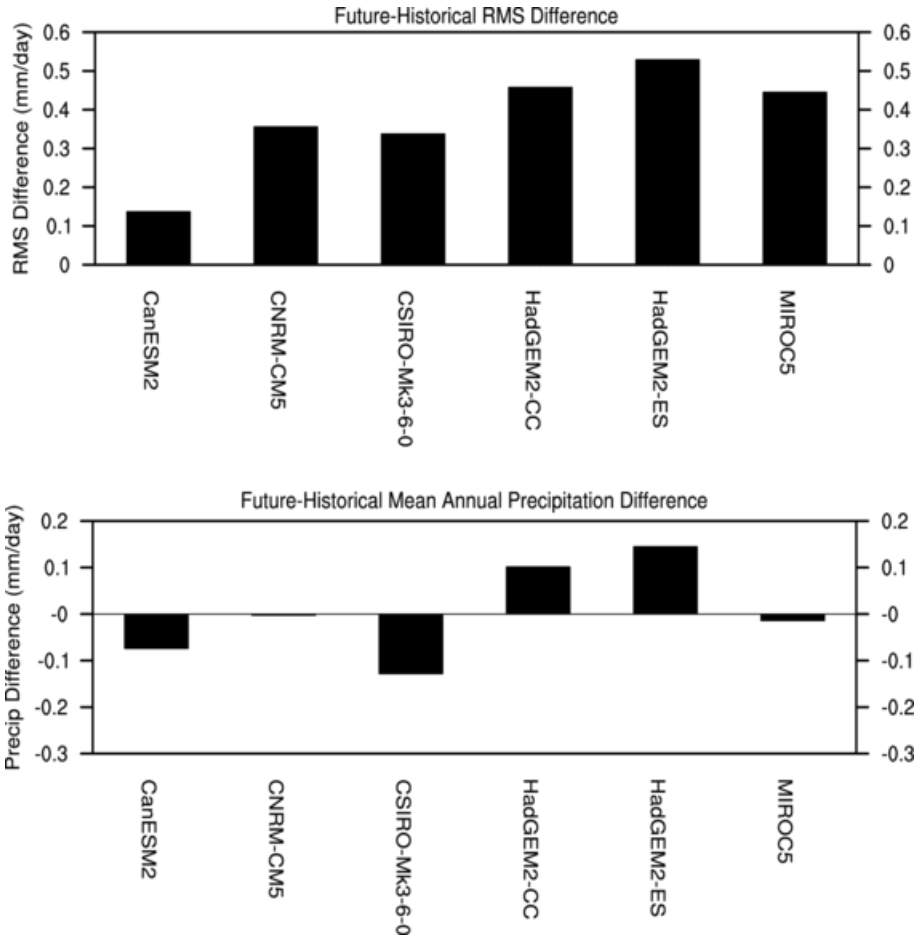

Figure 17. Bars represent the (a) RMS and (b) annual mean differences between the future (2071-2100) and historical (1979-2005) periods for the core NAM region (23^{o}N-30^{o}N, 105^{o}W-110^{o}W) for RCP4.5.

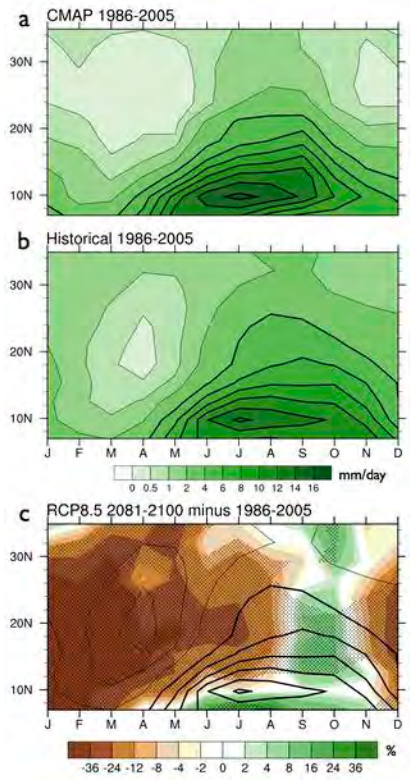

Figure 18. Precipitation annual cycle averaged for longitudes representing the North American Monsoon (102.5 to 115. W), for the 1986-2005 climatological period from CMAP precipitation, version 2 from Xie and Arkin 1997 (a) and the ensemble mean of 13 CMIP5 models (b), in units of mm/day with thick black lines identifying contours greater than 4 mm/day. Multi-model climatology contours (black lines) are reproduced in (c) which also shows ensemble mean precipitation % difference (colors). Areas of significant change are stippled. The models employed in the analysis are CCSM4, CNRM-CM5, CSIRO-Mk3, CanESM2, GFDL-CM3, GFDL-ESM2G, GISS-E2-R, IPSL-CM5A-LR, MIROC-ESM, MIROC5, MPI-ESM-LR, MRI-CGCM3, NorESM1-M.

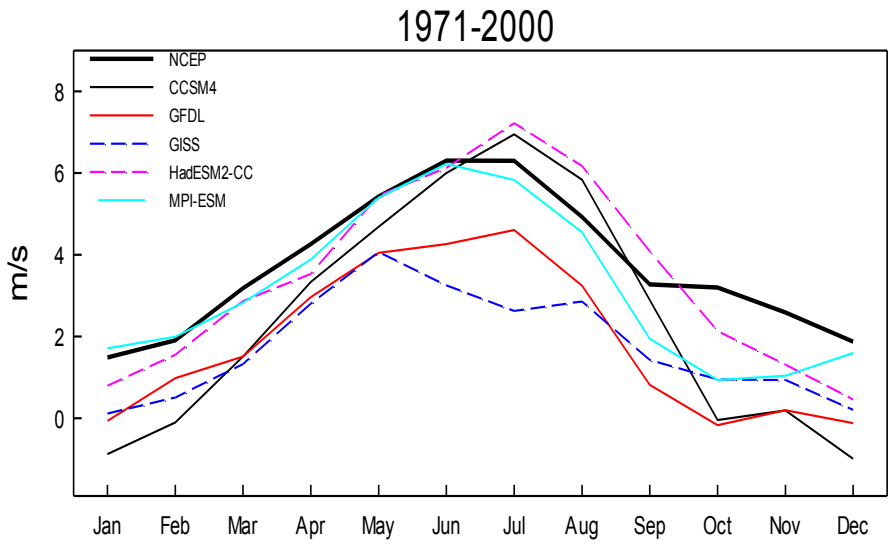

Figure 19. Climatology of LLJ strength as a function of month between 1971-2000 for NCEP-NCAR reanalysis and the CCSM4, GFDL, GISS, HadESM2-CC, and MPI-ESM models. The LLJ was computed as the 925 hPa meridional wind averaged over 27.5-32.5N and 95-100W.

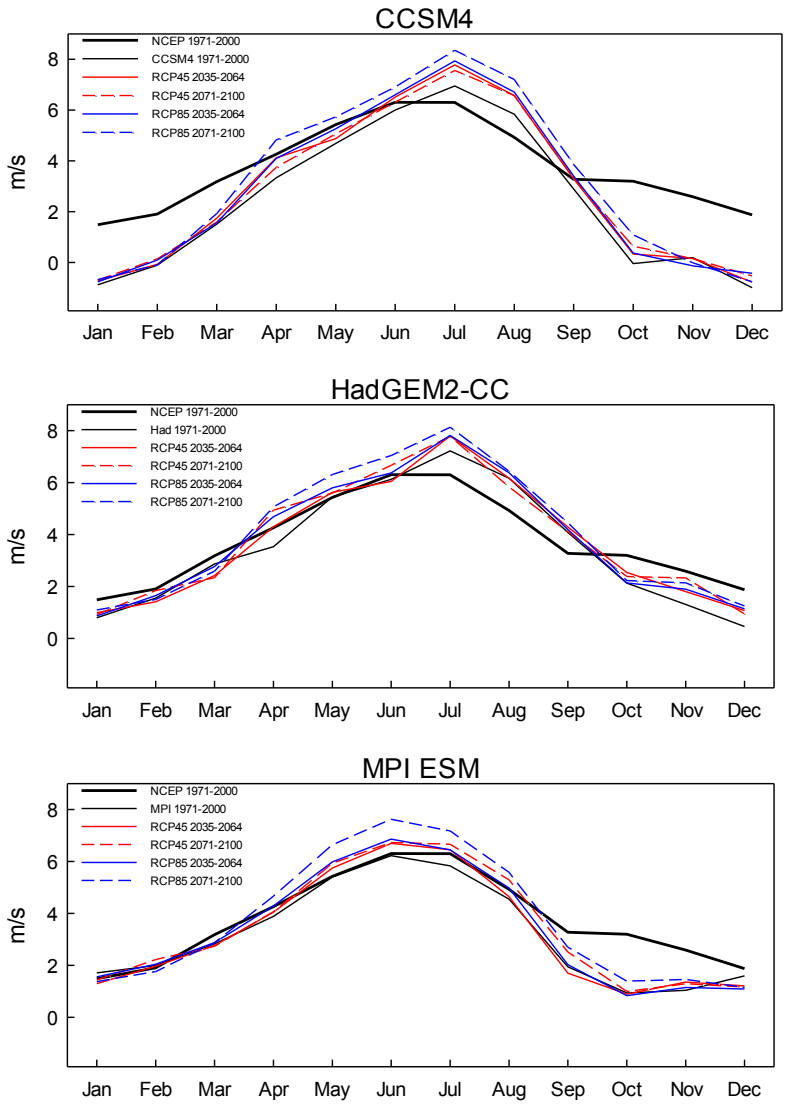

Figure 20. Monthly climatology of 925 hPa meridional wind averaged over 27.5-32.5N and 95-100W for 1971-2000, 2035-2064, and 2071-2100 for RCP4.5 and 8.5 for the CCSM4, HadGEM2-CC and MPI ESM models. The monthly climatology from NCEP-NCAR reanalysis during 1971-200 is shown on each plot.

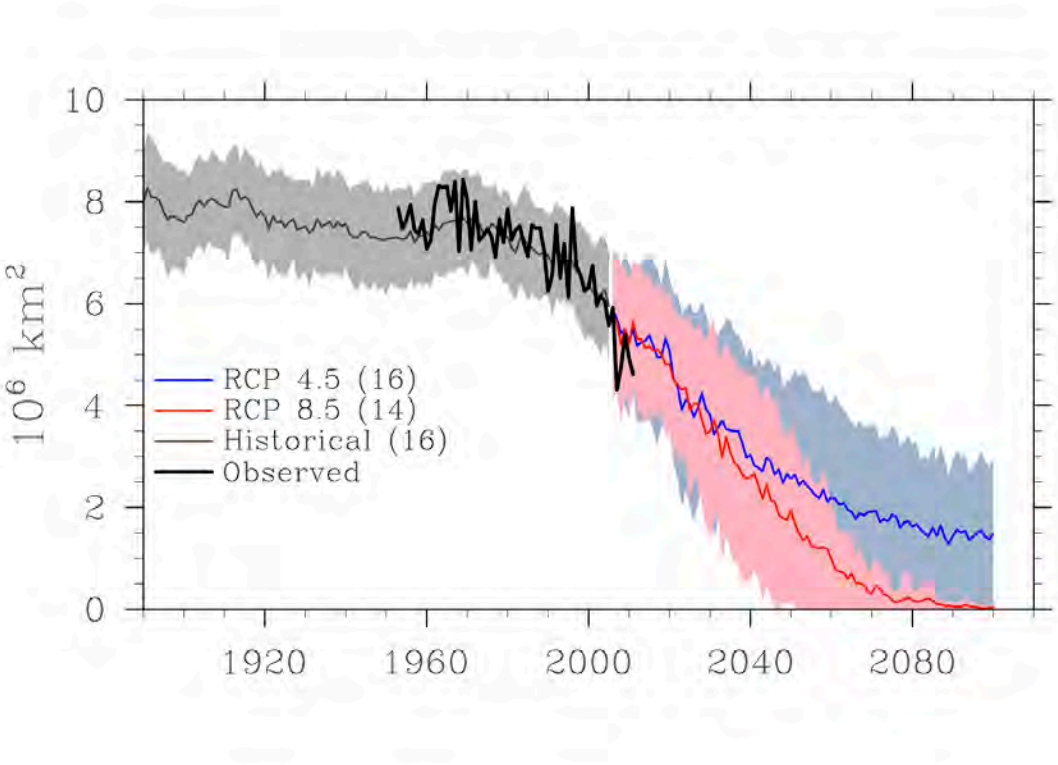

Figure 21. CMIP5 multi-model ensemble mean September Northern Hemisphere sea ice extent from 1900 to 2100, based on the historical (gray) and future RCP4.5 (blue) and RCP8.5 (red) emission scenarios. The observed ice extent from 1953-2011 is shown in black and the shading represents ± one standard deviation of the multi-model ensemble means. In deriving the multi-model ensemble mean for each emission scenario, only models that have at least 75% of their distribution of September ice extent within the observed range of 6.13 to 8.43x10^6 km^2 from 1953-1995 are included. The rejected models include CanESM2, GISS-E2-R, GISS-E2-H, CSIRO Mk3-6 and FGOALS-g2, resulting in a total of 16 models for the historical and RCP4.5 scenario and 14 models for the RCP8.5 scenario.

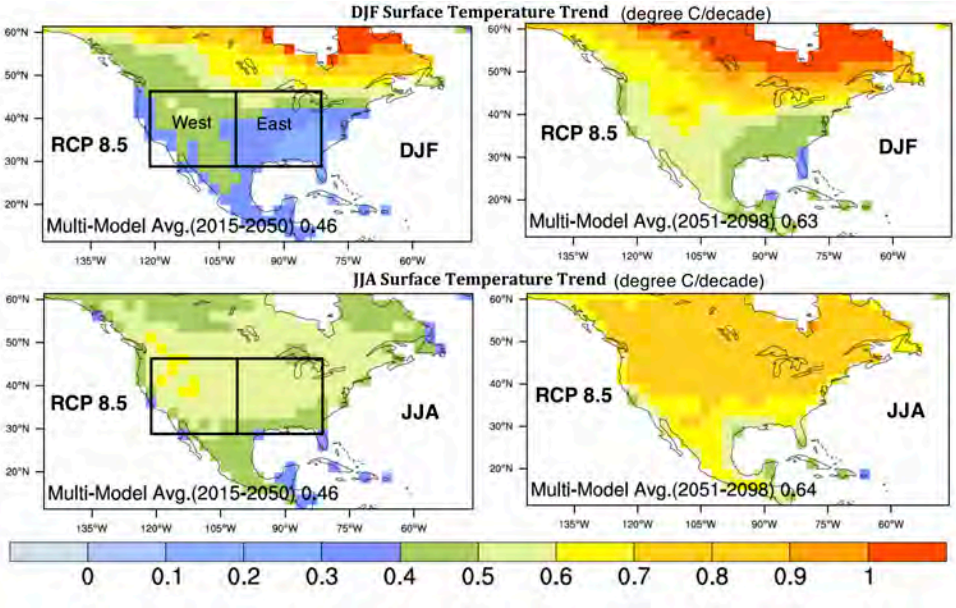

Figure 22. Winter and summer temperature trend in RCP8.5 for two time periods: (1) 2015-2050, (2) 2051-2098. Multi-model average is calculated from a total of 39 ensemble members from 16 climate models. Numbers in each panel show global mean temperature trend (land only, 60S to 60N).

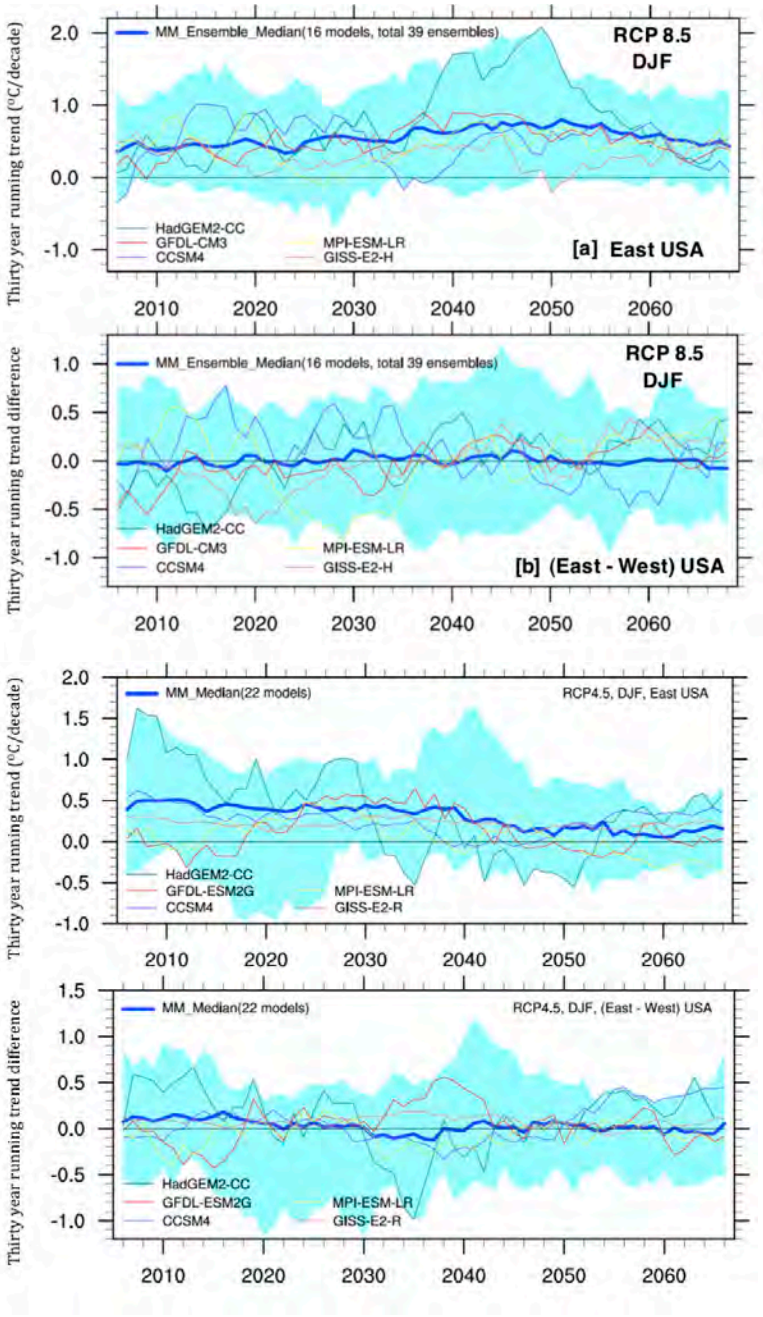

Figure 23. RCP 8.5 (a) 30 years running trend in East USA (defined in Figure 17) DJF Temperature Trend (b) 30 year running Trend difference between East and West USA. (c) and (d), same as (a) and (b), but for RCP4.5. The East and West USA are defined in Figure 16. Shaded region show 95% uncertainty range calculated from 39 ensemble members from 16 models in RCP 8.5 case, and from 22 models (ensemble average if model has more than one ensemble) in RCP 4.5 case. X-axis represents start of the 30 year period. For example, the trend corresponding to 2030 represent trend from 2030 to 2059. Five core models are also shown as an example, only the first ensemble member from each model in RCP 8.5 case, and ensemble average of each model in RCP 4.5 case.

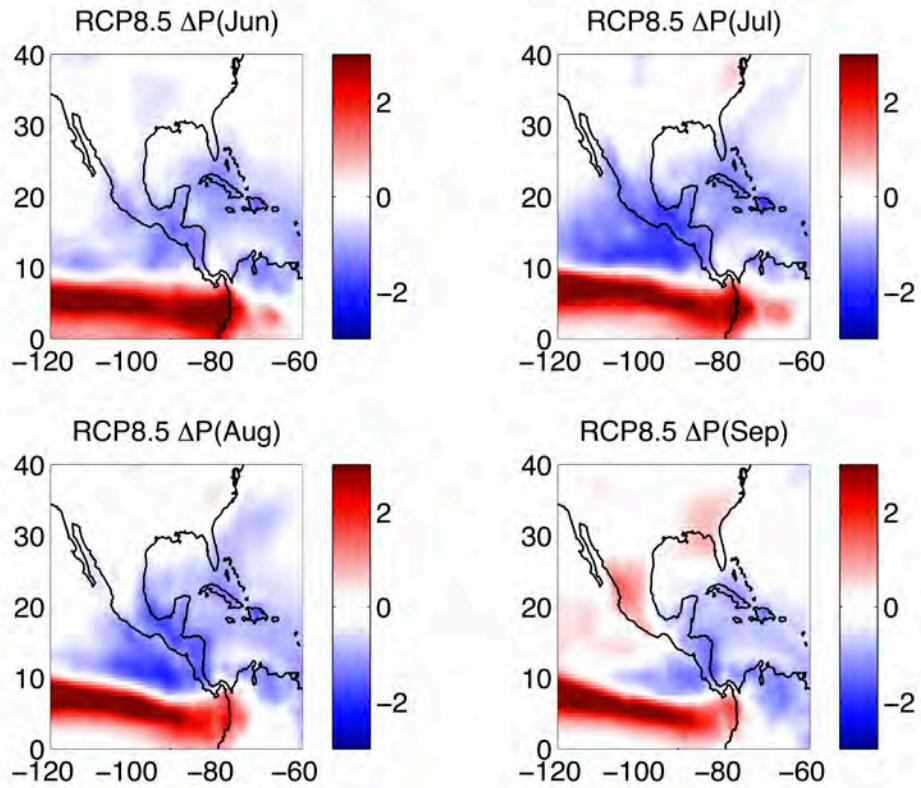

Figure 24. CMIP5 multimodel mean projection of precipitation change (mm/day) during each of the summertime months (June-September) based on the mean of the last two decades of the 21st century (2080-2099) of the RCP8.5 forcing experiment minus the mean over the historical experiment (1860-2005). The numbers of models included in the analyses are 23 and 20 for Historical and RCP8.5, respectively.

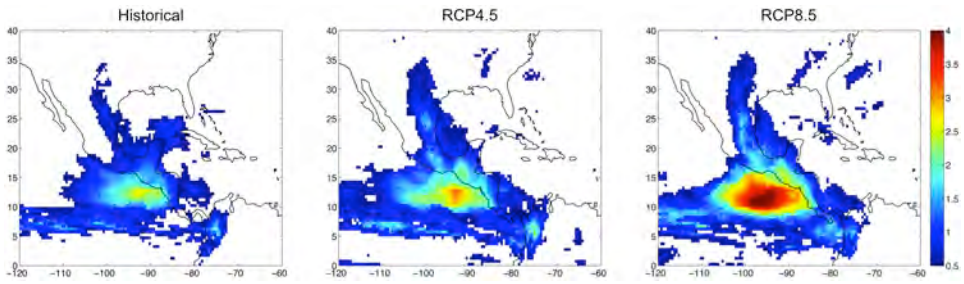

Figure 25. CMIP5 multimodel mean projection of the MSD (mm/day) averaged over the historical experiment, the RCP4.5 forcing experiment (2080-2099), and the RCP8.5 forcing experiment (2080-2099). The numbers of models included in the analyses are 23, 17, and 20 for Historical, RCP4.5, and RCP8.5, respectively.

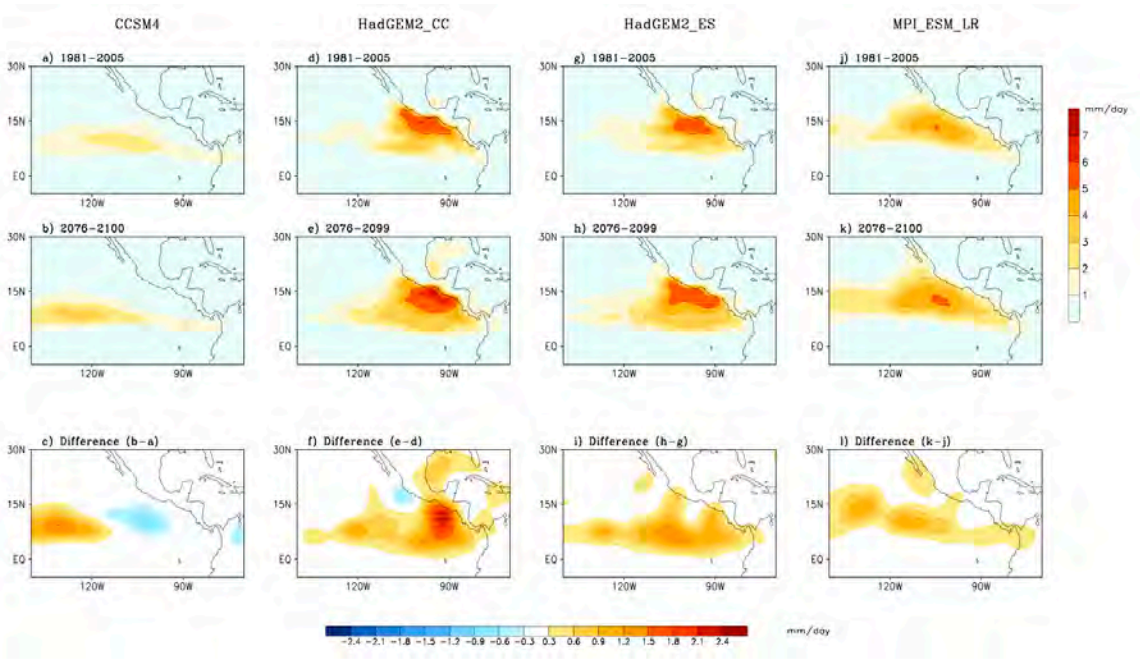

Figure 26. The leading complex EOF amplitude of 30-90 day precipitation anomalies during boreal summer during 1981-2005, 2076-2099 in RCP8.5, and the difference for the CCSM4, HadGEM2_CC, HadGEM2_ES, and MPI_ESM_LR models. The total variance explained by the leading CEOF mode for the end of the 20th Century and 21st Centuries are given as follows: CCSM4 (12.1%, 14%), HAD_GEM2_CC (22.1%, 25.7%), HAD_GEM2_ES (20.5%, 21.4%), MPI_ESM (25.1%, 26.4%). The color bar for the actual CEOF amplitudes are shown on the right, and the color bar for the difference is shown on the bottom. The time series of the CEOFs were normalized, and so amplitude information is contained in the spatial pattern.

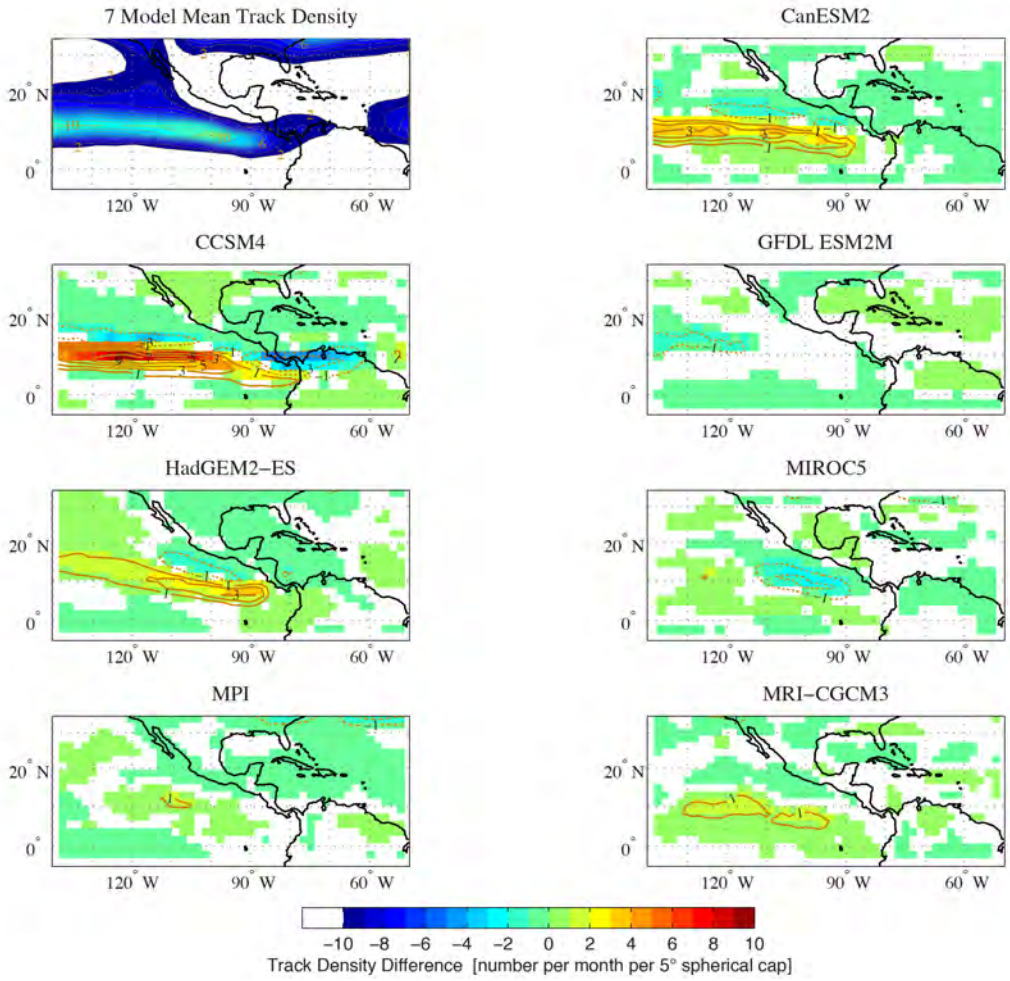

Figure 27. CMIP5 7-model mean track density for the RCP 4.5 future (May-Nov 2070-2100) projections. Contours every four density units starting with two. Also shown are the seven CMIP5 track density differences for the future minus historical (May-Nov 1979-2005) period. Colored areas indicate differences exceeding one standard error of the historical mean for that model. Contour lines are every one density unit with no zero contour shown.

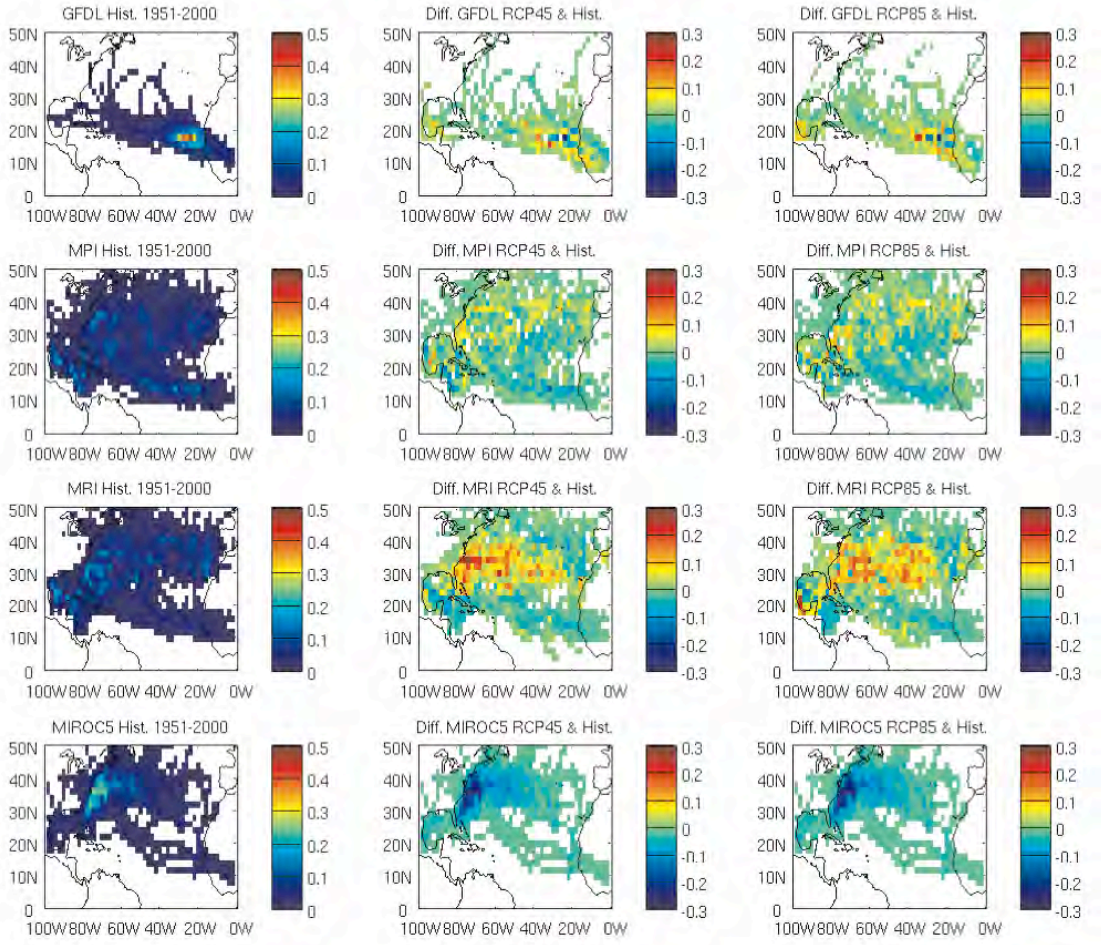

Figure 28. Left panels: mean track density in the North Atlantic for the historical simulation in the period 1951-2000 for the GFDL-ESM2M (1 ensemble member all pathways), MPI-ESM-LR (3 ens. Members all pathways), MRI (5 ens. members historical, 1 ens, member RCP4.5 and RCP8.5), and MIROC5(1 ens. member historical, 3 ens. members RCP4.5, 1 ens. member RCP8.5) models. The difference of the track density in the period 2051-2100 and historical track density is shown in the middle panels for RCP45 and the right panels for RCP85. The Camargo and Zebiak (2002) method defines the existence of a TC based on low-level vorticity, sea level pressure, definition of a warm core based on temperature anomalies, and surface wind speed. The storms also have to last at least 2 days to be considered in our analysis.

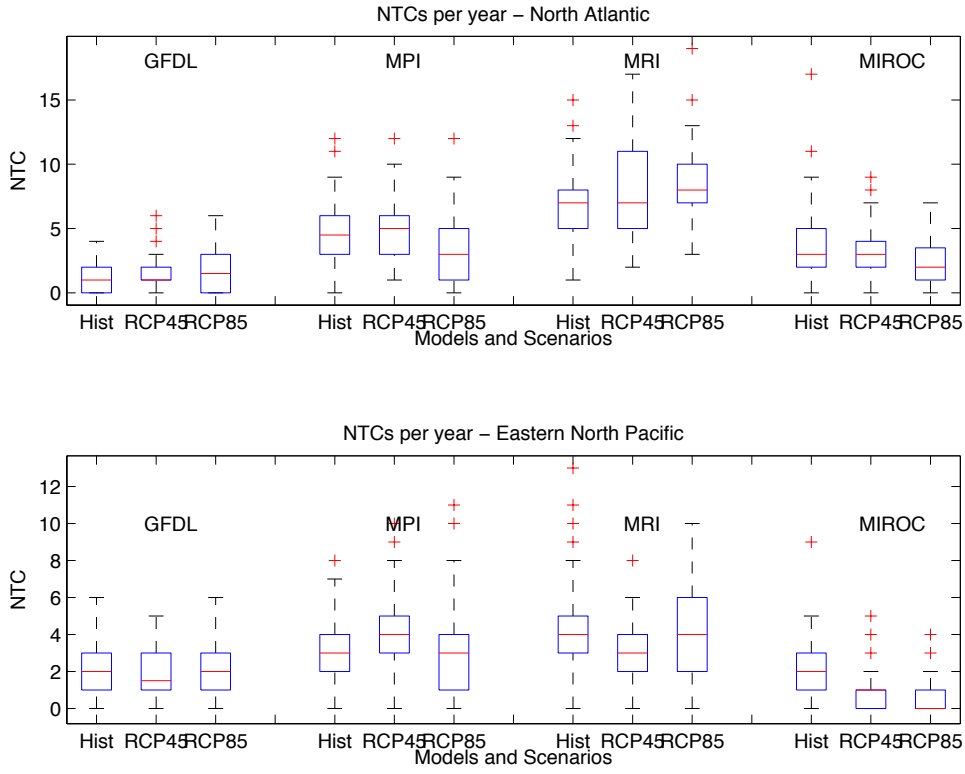

Figure 29. Box-plot distributions of the number of tropical cyclones (NTCs) per year in each model in the 3 different scenarios for the last 50 years in each century: historical (Hist, 1951-2000), RCP45 and RCP85 (2051-2100). The box denotes the range of the 25th and 75th percentiles of the distributions, while the median is marked by a red line. The values outside of the middle quartile are marked by whiskers and red crosses. We calculated the statistical significance of differences in the distributions of the number of TCs in the present and future using a Wilcoxon rank sum test for medians.

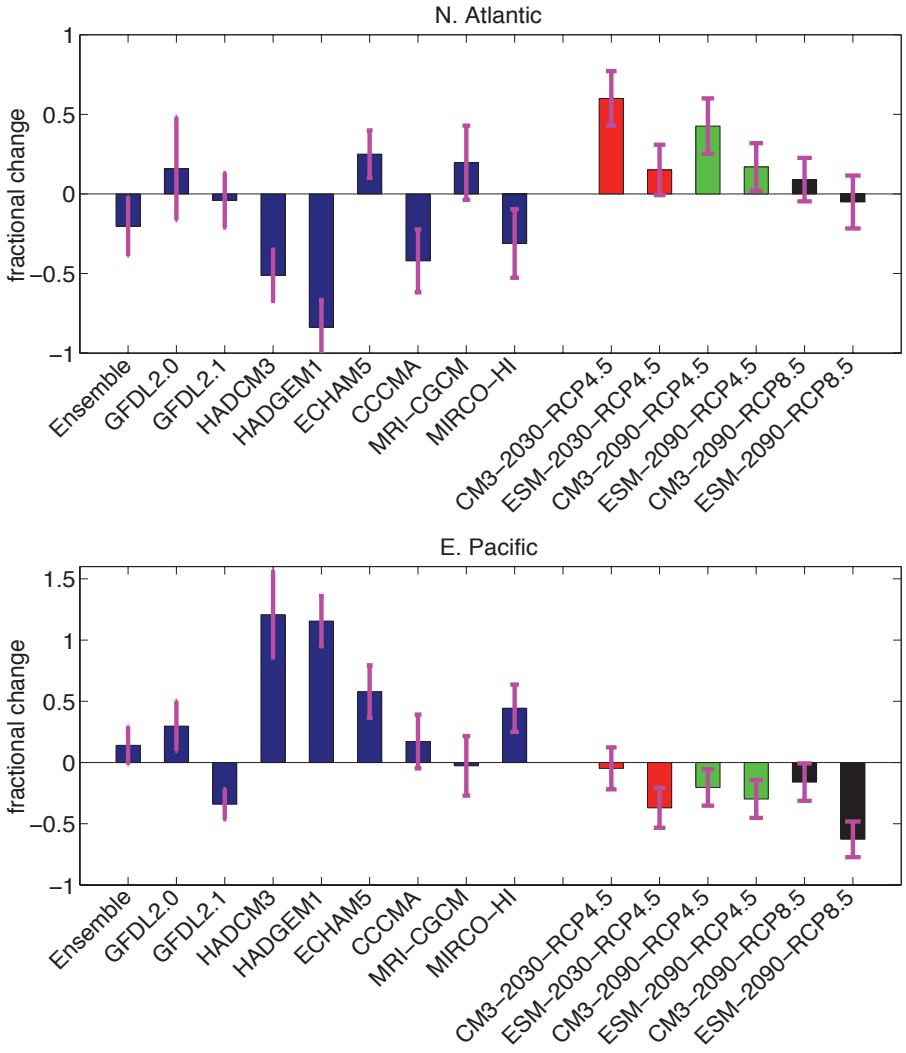

Figure 30. a) Fractional change in N. Atlantic hurricanes frequency downscaled using the GFDL C180HIRAM. Blue bars show results using the CMIP3 models projected SST warming anomalies (and their ensemble mean) at the late 21st century (2080-2100 relative to 2000-2020) for the A1B scenario. The control experiment was integrated for 20 years while most of the warming experiments were carried out for 10 years due to constraints of computer time. Red, green and black bars show results using GFDL CMIP5 model (CM3 and ESM) projected SST warming anomalies (CM3-2030-RCP4.5 and ESM-2030-RCP4.5: 2026-2035 averaged SST anomalies from CM3 and ESM RCP4.5 experiments with radiative gases at RCP4.5 2026-2035 values. CM3-2090-RCP4.5 and ESM-2090-RCP4.5: 2086-2095 averaged SST anomalies from CM3 and ESM RCP4.5 experiments with radiative gases at RCP4.5 2085-2095 values. CM3-2090-RCP8.5 and ESM-2090-RCP8.5: As in CM3-2090-RCP4.5 and ESM-2090-RCP4.5 experiments except using RCP8.5 model projected SST anomalies with

radiative gases at RCP8.5 2086-2095 values. The GFDL C180HIRAM present-day experiments contain a 3-member ensemble simulation for the period of 1981 to 2008. The CMIP5 SST anomalies are computed relative to 1981-2008 average. b) As in a) except for the E. Pacific.

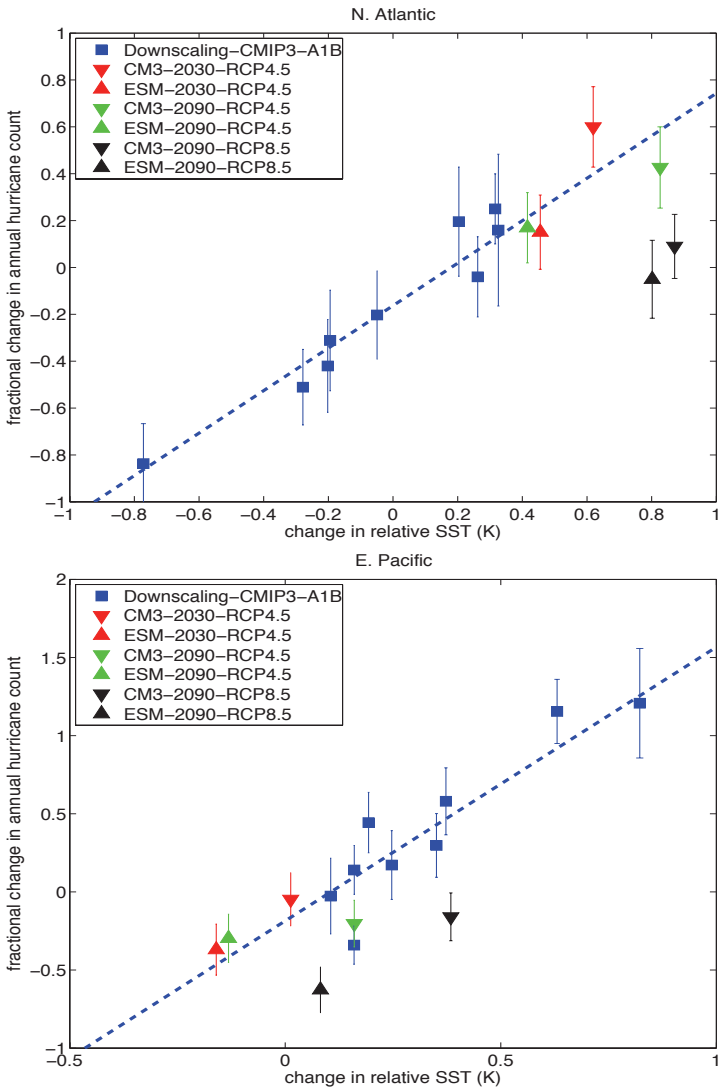

Figure 31. a) the fractional change in N. Atlantic hurricane frequency against changes in a relative SST index defined as the Atlantic Main Development Region (MDR) [80◦W-20◦W, 10◦N-25◦N] SST minus tropical mean [30S-30N] SST in ASO season. b) As in a) except for the E. Pacific, the E. Pacific Main Development Region is defined as [160◦W-100◦W, 7.5◦N-15◦N] .

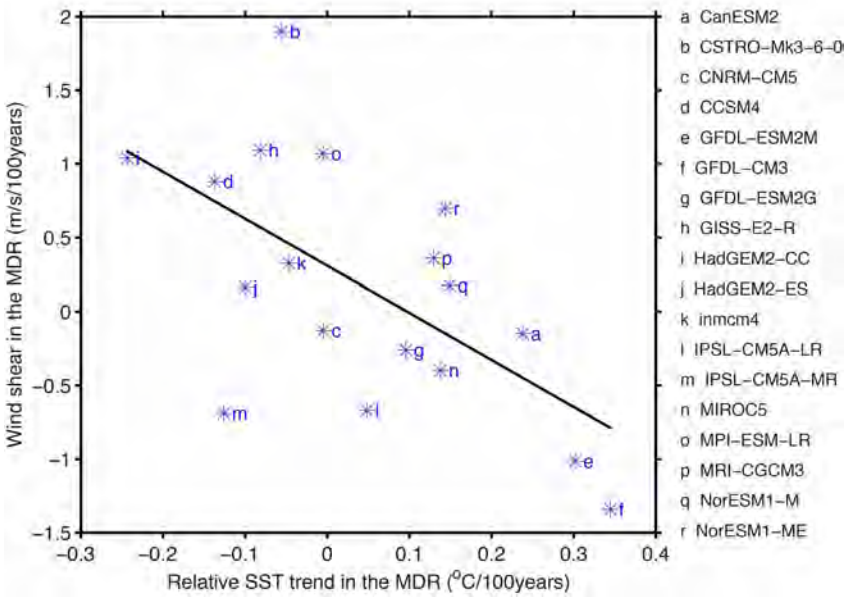

Figure 32. Scatterplot plot of the vertical wind shear trend versus the relative SST trend in the hurricane main development region (MDR; 85°W-15°W, 10°N-20°N) during the Atlantic hurricane season of June to November (JJASON). The relative MDR SST trend is calculated as the difference between the MDR SST trend and the global tropical (30°S-30°N) SST trend. SST is from the NOAA extended reconstructed SST version 3 (Smith et al. 2008).

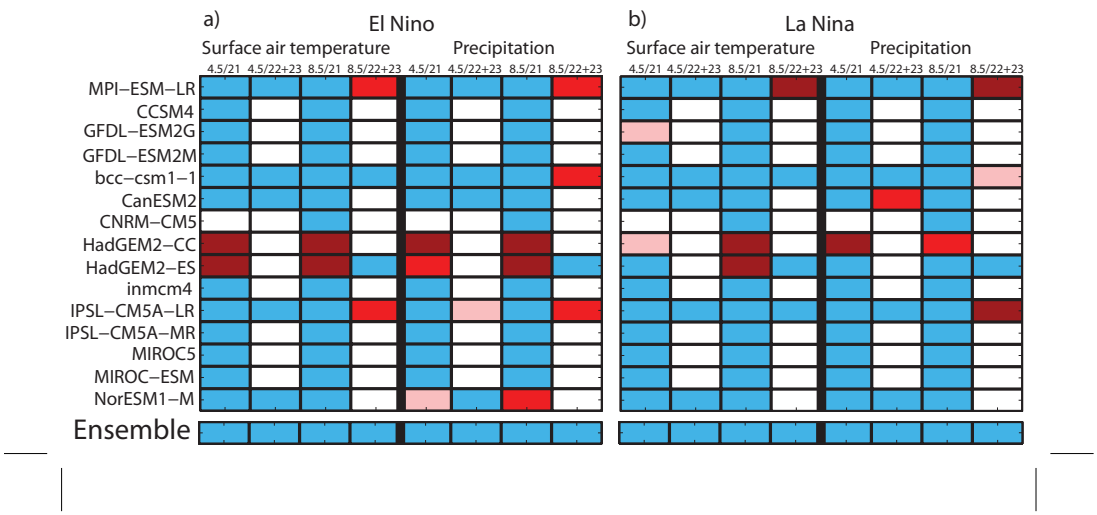

Figure 33. Field significance of the changes in (a) El Niño and (b) La Niña SAT (left columns) and precipitation (right columns) composites in CMIP5 models (rows) from the historical simulations to different epochs under two emissions scenarios. An El Niño (La Niña) episode is defined as all times such that the three-month running mean Niño3.4 SST, detrended and high-pass filtered in this case, is greater than 0.5°C (less than -0.5°C) for at least five consecutive three-month running seasons. The model names are given at the left, and the bottom row corresponds to the CMIP5 ensemble. Each column corresponds to a different variable, emissions scenario, and epoch, where the first number above the column indicates the emissions scenario and the second number indicates the epoch (e.g., "4.5/21" indicates RCP4.5 in the 21st century and "4.5/22+23" indicates RCP4.5 from 2101-2300). We determine that the model patterns are significantly different from the observed patterns if the patterns are statistically distinguishable in a test of field significance based on the "false discovery rate" (FDR) (Benjamini and Hochberg 1995, Wilks 2006). Light, medium, and dark red correspond with 90%, 95%, and 99% significance levels, respectively, blue corresponds with statistically insignificant ($\alpha_{global} > 0.1$) changes, and white indicates no available data.

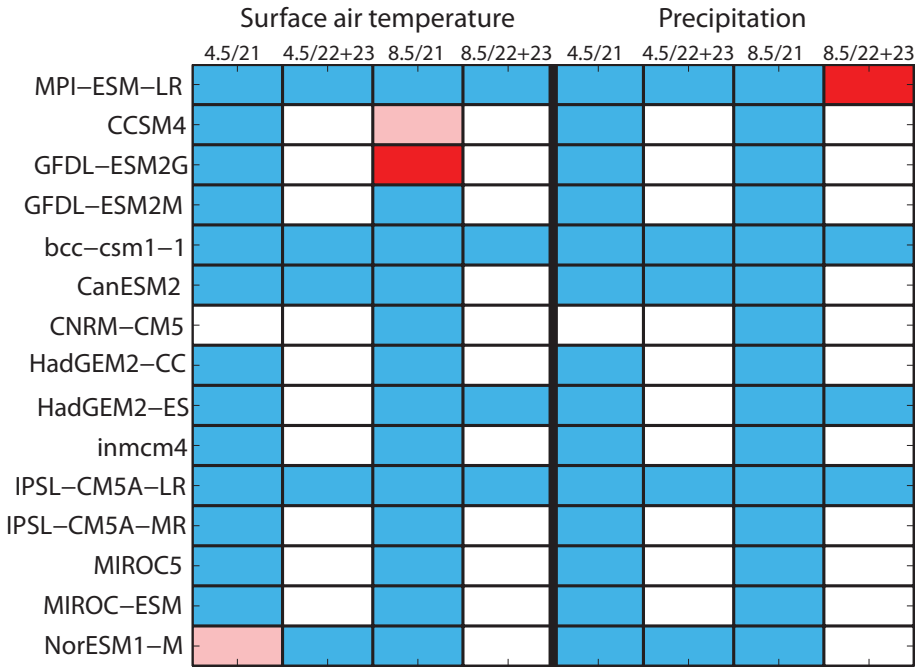

Figure 34. Field significance of the changes in PDO SAT (left columns) and precipitation (right columns) regressions in CMIP5 models (rows) from the historical simulations to different epochs under two emissions scenarios. The model names are given at the left, and the bottom row corresponds to the CMIP5 ensemble. Each column corresponds to a different emissions pathways and epoch, where the first number above the column indicates the emissions scenario and the second number indicates the epoch (e.g., "4.5/21" indicates RCP4.5 in the 21st century and 4.5/22+23 indicates RCP4.5 from 2101-2300). To assess significance, we regress detrended SAT and precipitation upon model PDO indices and then evaluate whether regression pattern changes are significant based on an FDR. Light, medium, and dark red correspond with 90%, 95%, and 99% significance levels, respectively, blue corresponds with statistically insignificant ($\alpha_{global} > 0.1$) changes, and white indicates no available data.

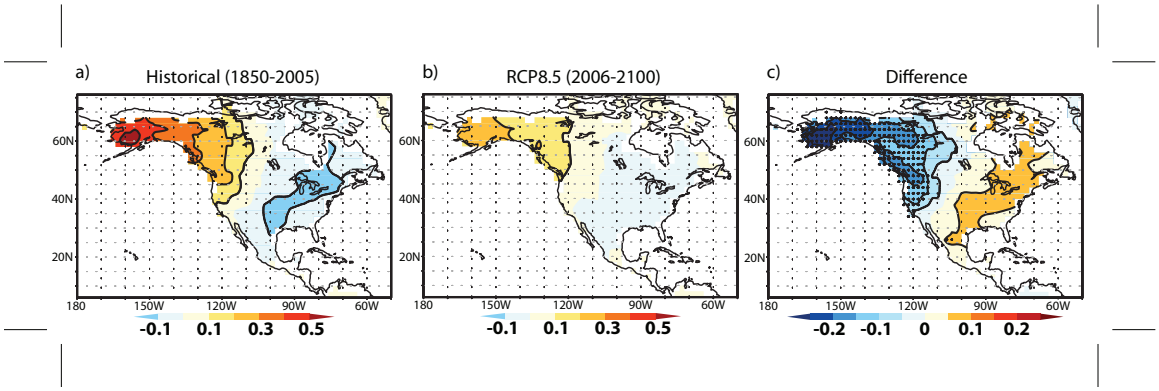

Figure 35. Ensemble regression of SAT anomalies with the PDO index during MAM in (a) historical simulations and (b) RCP8.5 simulations between 2006 and 2100, and (c) the difference between (a) and (b). The contour interval is 0.1°C in (a) and (b) and 0.05°C in (c). Stippling in (c) indicates where the differences are statistically significant at the 95% confidence level.